

RESEARCH ARTICLE

10.1029/2020JD032478

Key Points:

- Four components of radiation at different levels in the whole near-surface UBL were compared between clean and polluted episodes
- Relative to clean episode, the sensible heat flux was reduced more than net radiation in the near-surface UBL during heavy polluted episode
- Both weak thermal-forcing effects and weak dynamic motion contributed to the reduction in the sensible heat flux during pollution episodes

Supporting Information:

- Supporting Information S1

Correspondence to:

Z. Gao and Y. Yang,
zgao@mail.iap.ac.cn;
yyj1985@nuist.edu.cn

Citation:

Wang, L., Fan, S., Hu, F., Miao, S., Yang, A., Li, Y., et al. (2020). Vertical gradient variations in radiation budget and heat fluxes in the urban boundary layer: A comparison study between polluted and clean air episodes in Beijing during winter. *Journal of Geophysical Research: Atmospheres*, 125, e2020JD032478. <https://doi.org/10.1029/2020JD032478>

Received 31 JAN 2020

Accepted 13 MAY 2020

Accepted article online 18 JUN 2020

Author Contributions:

Conceptualization: Linlin Wang, Zhiqiu Gao

Data curation: Fei Hu, Shiguang

Miao, Junkai Liu, Changwei Liu

Formal analysis: Linlin Wang,

Yuanjian Yang

Methodology: Sihui Fan, Aqiang

Yang, Shanshan Chen

Software: Zexia Duan

Writing - original draft: Linlin Wang

Writing - review & editing: Yubin Li, Zhiqiu Gao, Yuanjian Yang

Vertical Gradient Variations in Radiation Budget and Heat Fluxes in the Urban Boundary Layer: A Comparison Study Between Polluted and Clean Air Episodes in Beijing During Winter

Linlin Wang^{1,2}, Sihui Fan^{1,2}, Fei Hu¹ , Shiguang Miao³ , Aqiang Yang⁴ , Yubin Li² , Junkai Liu¹, Changwei Liu² , Shanshan Chen⁵, Hung Chak Ho⁶ , Zexia Duan^{1,2}, Zhiqiu Gao¹ , and Yuanjian Yang² 

¹State Key Laboratory of Atmospheric Boundary Layer Physics and Atmospheric Chemistry (LAPC), Institute of Atmospheric Physics, Chinese Academy of Sciences, Beijing, China, ²Collaborative Innovation Centre on Forecast and Evaluation of Meteorological Disasters, School of Atmospheric Physics, Nanjing University of Information Science and Technology, Nanjing, China, ³Institute of Urban Meteorology, China Meteorological Administration, Beijing, China, ⁴Institute of Remote Sensing and Digital Earth, Chinese Academy of Sciences, Beijing, China, ⁵Institute of Remote Sensing and Geographic Information System, Peking University, Beijing, China, ⁶Department of Urban Planning and Design, The University of Hong Kong, Hong Kong, China

Abstract Previous studies have reported air pollution-radiation interactions in the urban boundary layer (UBL), but vertical gradient variations in the radiation budget and heat flux under air pollution conditions are relatively sparse. In this study, based on gradient observations from the Beijing 325 m meteorological tower in December 2015, the characteristics of near-surface radiation balance and energy budget at three levels under different pollution conditions were comparatively investigated. Relative to clean days, both downward and upward shortwave radiation (DSR and USR) dropped during daytime, while downward and upward longwave radiation (DLR and ULR) enhanced during nighttime on heavily polluted days, showing that with evaluated height, the drop magnitudes of DSR and USR decreased, while the enhancement magnitude of DLR (ULR) decreased (increased). The combined effects of four radiation components significantly induced the reduction in net radiation (R_n) on polluted days, leading to the near-surface energy budget change. In addition, the monthly averaged anthropogenic heat flux (Q_p) was estimated to quantitatively calculate the heat storage (G) term in the surface energy budget. During daytime, compared to the clean episodes, the sensible heat flux (H) was reduced more than R_n in the whole near-surface UBL during heavy polluted episodes, resulting in smaller $H/(R_n + Q_p)$ and larger $G/(R_n + Q_p)$. Finally, we revealed that weak thermal forcing effects caused by insufficient availability of net radiation energy at the surface and weak dynamic motion associated with weak winds were both responsible for the larger reduction (increase) in H (G) during pollution episodes in the whole near-surface UBL.

1. Introduction

The heat exchange process is one of the most fundamental factors in the surface energy balance for understanding the development and variations in the atmospheric boundary layer, urban air pollution episodes, the thermal environment, and the resultant human health (Gu et al., 2018; Oke et al., 2017; Wang & Li, 2019; Yim et al., 2019; Zheng et al., 2018); additionally, this understanding is also critical for improving numerical weather and climate models as well as air quality models (Chen & Dudhia, 2001; Holt et al., 2006; Miao et al., 2009; Li & Bou-Zeid, 2014; Liu et al., 2018; Sellers et al., 1996).

Solar radiation is the most important driver of surface energy balance (Haywood, 2011). Previous studies have reported that radiative transfer processes can be affected by air pollution through the scattering, reflection, and absorption of shortwave radiation and through the reflection, absorption, and emission of longwave radiation (Brown et al., 2018; Dickerson et al., 1997; Haywood & Boucher, 2000; Jacobson et al., 2007; Wang et al., 2014, 2016), which affects the surface energy balance. Oke et al. (2017) stated that many air pollutants, fine particulate matter in particular, modify radiative transfer processes, which impacts airflow over longer time scales. In recent years, the aggravation of air pollution induced by massive

emissions and unfavorable meteorological conditions in China (Guo et al., 2011, 2016; Li et al., 2017; Miao et al., 2015; Wang et al., 2012; Yang et al., 2018), especially in urban areas, largely affects the variations in solar radiation and associated radiation budget at both the weather and climatic scales, resulting in obvious weather and climate effects (Che et al., 2005; Fu et al., 2017; Guo et al., 2019; Haywood, 2016; Hu & Liu, 2013; Johnson et al., 2019; Wang et al., 2018; Zhang et al., 2013, 2018). However, studies on how the urban boundary layer (UBL) heat exchange responds to the various radiation budgets at different vertical heights under air pollution conditions are less studied.

Beijing, the capital of China, is among the fastest growing cities in the world during the past decades. Rapid urbanization has resulted in numerous environmental problems, such as air pollution. Previous studies have reported that heavy pollution in Beijing is strongly related to local meteorological conditions, especially UBL processes (Chan & Yao, 2008; Ling et al., 2014; Shi et al., 2019; Su et al., 2018; Wang, Liu, et al., 2019; Wang, Wang, et al., 2019; Zhang et al., 2012). In addition, in response to reduced solar radiation, the cooling of surface air temperature can lead to strong temperature inversions in the near-surface layer, which can increase the atmospheric stability and then prolong the accumulation of pollution (Barbaro et al., 2013; Lolli et al., 2019; Tang et al., 2016; Wu et al., 2019). Particularly strong interactions were verified in the Beijing area when the $PM_{2.5}$ (fine particulate matter with a diameter smaller than $2.5 \mu\text{m}$) concentrations were larger than $150\text{--}200 \mu\text{g m}^{-3}$ (Luan et al., 2018). Recently, based on a case observation from a 325 m meteorological tower in a heavily polluted, high-density building area of Beijing during 1–4 December 2016, Wang, Liu, et al. (2019) found that vertical mixing could be weakened by large aerosol radiation cooling effects related to increased pollutants and further worsen the pollution, leaving large gaps in how different radiation budget processes under different pollution conditions modulate the heat flux in the vertical direction in urban areas.

For this study, we aim to comprehensively investigate the characteristics of heat flux in the urban boundary layer during polluted and clean air episodes in Beijing from 1 to 31 December 2015 by using 325 m meteorological tower and conventional meteorological observations from the urban center of Beijing, China. The organization of this paper is as follows: In section 2, the observational site, sensors, and data processing procedures are described. In section 3, the meteorological factors at 15 height levels, radiative transfer at three height levels, and heat transfer at seven height levels in the UBL over Beijing under different polluted (clean, light polluted, and heavy polluted) conditions are compared. The conclusions are given in section 4.

2. Materials

2.1. Site and Data

The main data used in this study were from the Beijing 325-m meteorological tower (Figure 1a), which is located at an urban site at the Institute of Atmospheric Physics (IAP), Chinese Academy of Sciences (39.97°N , 116.37°E ; Beijing “inner city” site) (Figure 1b). Within a 5 km radius of the tower, buildings of different heights are distributed irregularly in all directions, and the area is surrounded by four-story to 20-story buildings with heights of 10–60 m (Liu et al., 2017) and mean heights of 18.7 m ($4 \text{ km} \times 4 \text{ km}$) and 19.1 m ($20 \text{ km} \times 20 \text{ km}$) based on the ground survey (Miao et al., 2012). In the present study, we just examine the differences in radiation budget and heat fluxes between the selected clean and pollution cases during 1–31 December 2015. Nevertheless, the selected episodes covered in December as a representative month for winter can to a certain extent remove the influence of solar zenith angle and intra-seasonality.

Sonic anemometers (Model Windmaster Pro, Gill, UK) are settled at seven different levels of this tall tower to obtain turbulent flux measurements, including the streamwise (u), cross-stream (v), vertical velocities (w), and the virtual air temperature (T_v). The downward shortwave radiation (DSR), upward shortwave radiation (USR), downward longwave radiation (DLR), and upward longwave radiation (ULR) measurements are collected using the downward-pointing and upward-pointing pyrgeometers and pyranometers (CNR1, Kipp & Zonen, Netherlands) at three different levels to measure four-component radiation. Meteorological elements, including wind speed (WS), wind direction, air temperature (T), and relative humidity (RH), are measured at 15 levels above ground. The main sensors erected at the 325 m tower are summarized in Table 1. Additionally, the near-surface WS (05103-L, R. M. Young) and temperature (HMP45C, Vaisala) at the 2.2 m level are measured at a surface station approximately 20 m south of the tower. Using Tapered Element Oscillating Microbalance analyzers with hourly monitored readings, the mass concentrations of $PM_{2.5}$ measured at the Beijing Olympic Sports Center (Aoti surface station, approximately 2 km north of

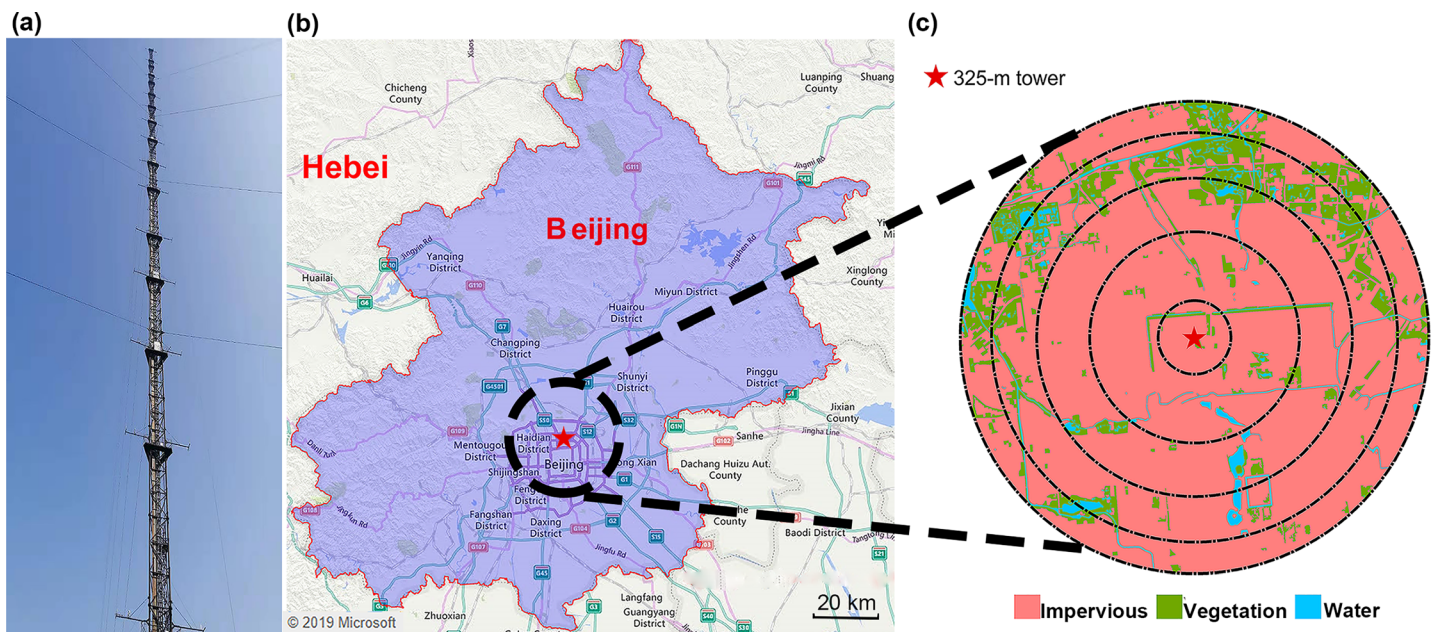


Figure 1. Photograph of the 325 m tower (a), the geographical location of the 325 m tower at the IAP site (courtesy of Bing, © 2019 Microsoft) (b), and the impervious surface fraction retrieved from a Landsat satellite image in 2015 (c). The circles roughly indicate the footprints of measurements at different heights (Red star: 325 m tower).

IAP station) were obtained from the website of the China National Environmental Monitoring Center (<http://113.108.142.147:20035/emcpublish>).

2.2. Methods

2.2.1. Footprint of Site

Due to the importance of ensuring sufficient spatial representativeness of the eddy-covariance fluxes, especially on the complex urban surface, a quantitative description of the scalar flux footprint is essential. The average footprints of the study sites were determined in a previous study (Cheng et al., 2018) using an approximate analytical model based on a combination of Lagrangian stochastic dispersion model results and dimensional analysis (Hsieh et al., 2000). The average fetch length was estimated as 238.0, 589.0, 2,644.0, 7,617.0, 11,461.0, 14,746.0, and 17,013.0 m at heights of 8, 16, 47, 80, 140, 200, and 280 m, respectively, in Cheng et al. (2018). Based on these results, we estimated the land cover fractions retrieved from a Landsat 8 satellite image in 2015 (with a resolution of 30 m), and the circles shown in Figure 1c roughly indicate the footprints of the measurements at different heights. With these circular footprints, the distribution of the flux source area can be directly determined. The compositions in the footprints of the 325 m tower were separated into three categories: impervious (including both ground and buildings), vegetation, and water. Note that the fetch lengths of 8 and 16 m were so small that the satellite image could not provide reliable land cover fractions, so only the other five land use fractions within the footprint measured heights are given in Table 2. As shown in Table 2, impervious built-up surfaces were the dominant land cover type. Even for the 280 m level, the fraction was 83.1%, and for the 47, 80, and 140 m levels, the fraction exceeded 90%, indicating high-density buildings underlying the surface around the IAP site in the center of Beijing.

Table 1
Key Technical Specifications of the Sensors on the 325 Tower

Sensor type	Measurement	Unit	Sampling frequency	Installation height (m)
CNR1	DSR/USR DLR/ULR	$W^{-1} m^{-2} W^{-1} m^{-2}$	0.1 Hz	47/140/280
010C	WS	$m s^{-1}$	0.1 Hz	8/15/47/65/80/100/120/140/160/180/200/240/280/320
HMP54C	T RH	$^{\circ}C \%$	0.1 Hz	8/15/47/65/80/100/120/140/160/180/200/240/280/320
Gill	$u/v/w T_v$	$m s^{-1} ^{\circ}C$	10 Hz	8/16/47/80/140/200/280

Table 2
Land Use Fractions Within the Footprints of Each Flux Measurement Height at the 325 m Tower Site

Height (m)	Impervious (%)	Vegetation (%)	Water (%)
47	91.6	7.7	0.7
80	93.3	4.9	1.8
140	92.1	5.7	2.3
200	84.7	12.0	3.3
280	83.1	13.4	3.5

Vegetation was the second most common surface type, and the maximum fraction in these five footprints was only 13.4% for the 280 m level. The water surface had the lowest fractions, and the fractions in these five footprints increased with measured levels, varying from 0.7% to 3.5%.

2.2.2. Calculation of Heat Flux

The friction velocity u_* (m s^{-1}), turbulence kinetic energy TKE per unit mass of flow ($\text{m}^2 \text{s}^{-2}$), sensible heat flux (H), and latent heat flux (LE) were calculated as follows:

$$u_* = \left(\overline{u'w'^2} + \overline{v'w'^2} \right)^{1/4} \quad (1)$$

$$\text{TKE}/m = \frac{1}{2} \left(\overline{u'^2} + \overline{v'^2} + \overline{w'^2} \right) \quad (2)$$

$$H = \rho C_p \overline{w'T_v'} \quad (3)$$

$$LE = L_v \overline{w'q'} \quad (4)$$

where ρ is the air density (kg m^{-3}), C_p is the specific heat capacity at a constant pressure ($\text{J kg}^{-1} \text{K}^{-1}$), T_v is the virtual air temperature (K), L_v is the latent heat of water vaporization (J kg^{-1}), and q is the specific humidity (kg kg^{-1}).

The three-dimensional sonic anemometer original records (10 Hz) were processed prior to analysis using the methods of double rotation (i.e., yaw and pitch rotations) and linear detrending. The overbar denotes time averages, and an averaging period of 1 hr was used in this study. The density effect correction by Detto and Katul (2007) was used in this paper. In addition, the planar fit method (Wilczak et al., 2001) was used to determine the plane to correct the tilt of the anemometer.

The surface energy budget (SEB) over urban surfaces is formulated as

$$R_n + Q_f = H + LE + G \quad (5)$$

where G is the ground and urban canopy heat storage. The net radiation R_n is described as

$$R_n = \text{DSR} - \text{USR} + \text{DLR} - \text{ULR} \quad (6)$$

The additional energy released by the anthropogenic heat flux (Q_f) due to human activities is a significant term in urban areas, which can be defined as a measurement of the heat released into the environment by human activities, that is, anthropogenic heat emissions generated per unit time and area at regional or even global scales (Chen et al., 2014; Chen & Hu, 2017; Chen & Shi, 2012; Taha, 1997). Sources of anthropogenic heat include industrial activities, heating and cooling of buildings, human metabolism, and vehicle exhaust, which play important roles in weather and climate processes and associated model simulations and developments (Chen et al., 2016, 2014). In this study, Q_f was estimated with satellite data using the RAHF (Refined Anthropogenic Heat Flux) model, which can clearly demonstrate the spatial distribution of Q_f at a 500 m resolution based on multisource remote sensing data and energy consumption statistics (Chen, Hu, et al., 2019; Chen & Hu, 2017). Heat storage is difficult to measure directly, requiring extensive observations that cover the diversity of buildings, canyons, and other elements in the urban canopy volume (Kotthaus & Grimmond, 2014). Thus, the heat storage term G estimated by the energy balance residual approach, that is, $R_n + Q_f - H - LE$, will be analyzed in this work.

3. Results and Discussion

3.1. Characteristics of Surface Meteorological Conditions

In this study, the environmental air quality criteria issued by the Ministry of Environmental Protection of China were used to categorize the pollution conditions. Three levels were identified as follows: clean days, light polluted days, and heavy polluted days with daily mean $\text{PM}_{2.5}$ concentrations ranging from 0 to $75 \mu\text{g m}^{-3}$, 75 to $150 \mu\text{g m}^{-3}$, and above $150 \mu\text{g m}^{-3}$, respectively. The selected period covered 1 month

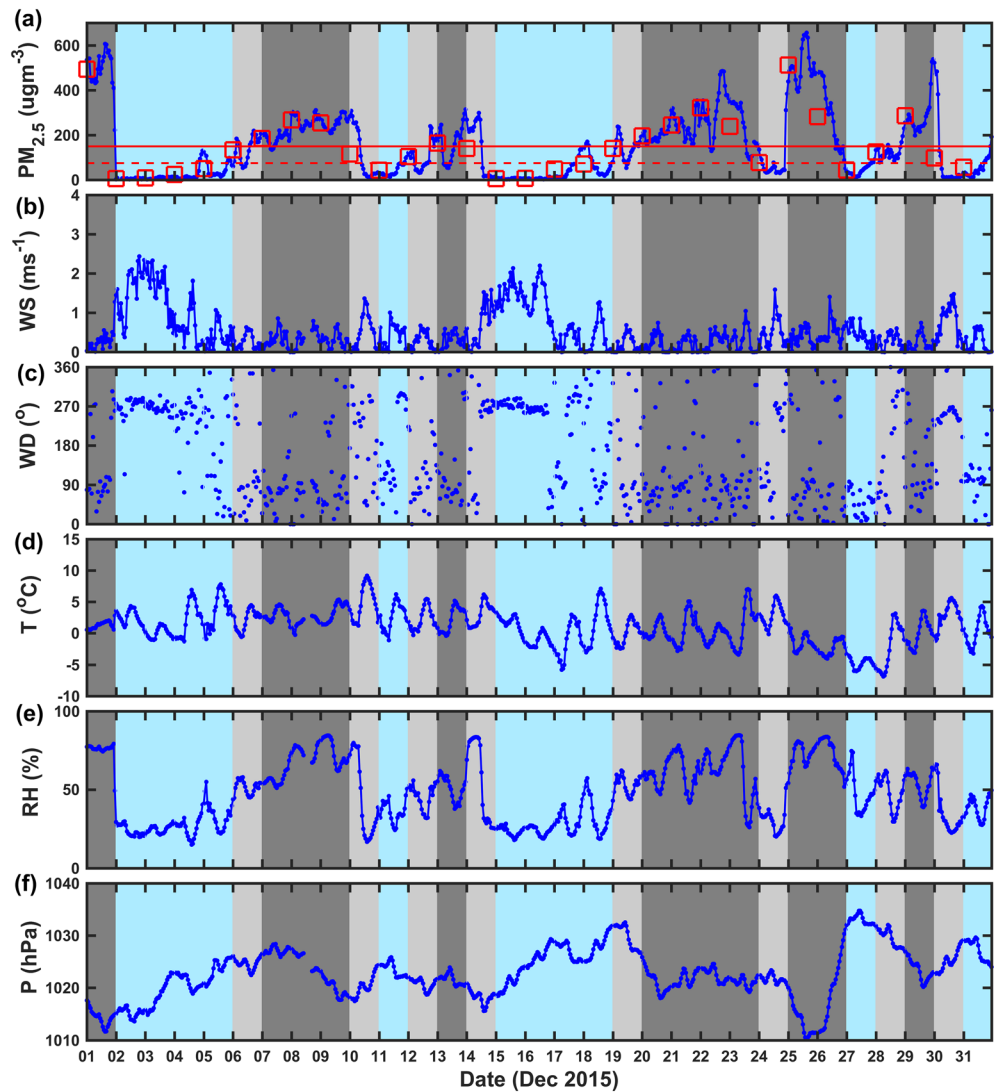


Figure 2. The time series of surface $PM_{2.5}$ concentrations at the Aoti surface station (a), surface WS (b), wind direction (c), air temperature (d), RH (e), and pressure (f) during the period from 1 to 31 December 2015 at the IAP site. The light blue, light gray, and dark gray shades mark clean, light polluted, and heavy PEs, respectively (red square: daily averaged $PM_{2.5}$ concentration, dashed and closed red lines: $PM_{2.5}$ concentrations that are equal to $75 \mu\text{g m}^{-3}$ and $150 \mu\text{g m}^{-3}$, respectively).

from 1 to 31 December 2015, as shown in Figure 2a, indicating that pollution episodes frequently occurred, and in some episodes, the daily maximum and mean values reached approximately 500 and $650 \mu\text{g m}^{-3}$, respectively. Finally, 11 clean days (clean episodes, CEs), eight light polluted days (light polluted episodes, LPEs), and 12 heavy polluted days (heavy polluted episodes, HPEs) were obtained during this 1 month. These 20 polluted days were named polluted episodes (PEs).

As shown in Figure 2, wind speed was ranged as $1-3$, $0.5-2$, and $0-1 \text{ m s}^{-1}$ for CEs, LPEs, and HPEs, respectively. The wind direction was mostly northerly for CEs, while had not obvious systematic features for polluted days. This is mainly resulted of this weak wind direction at 2-m level for polluted days can easily disturbed by the surrounding buildings. Therefore, Figure 3 shows that 24-hr back trajectories of the different polluted days (Figure 3) at 100 m on 17:00 LST (the most occurrence time for pollution events), indicating that the air masses were mostly from the northwest and moved faster during CEs. Compared to CEs, air masses moved slower for LPEs, and the slowest for HPEs, which more originated from southwest, indicating that the regional transport from the heavily southern Hebei Province to Beijing played an essential role in the formation of the severe haze events in Beijing during PEs, especially for HPEs.

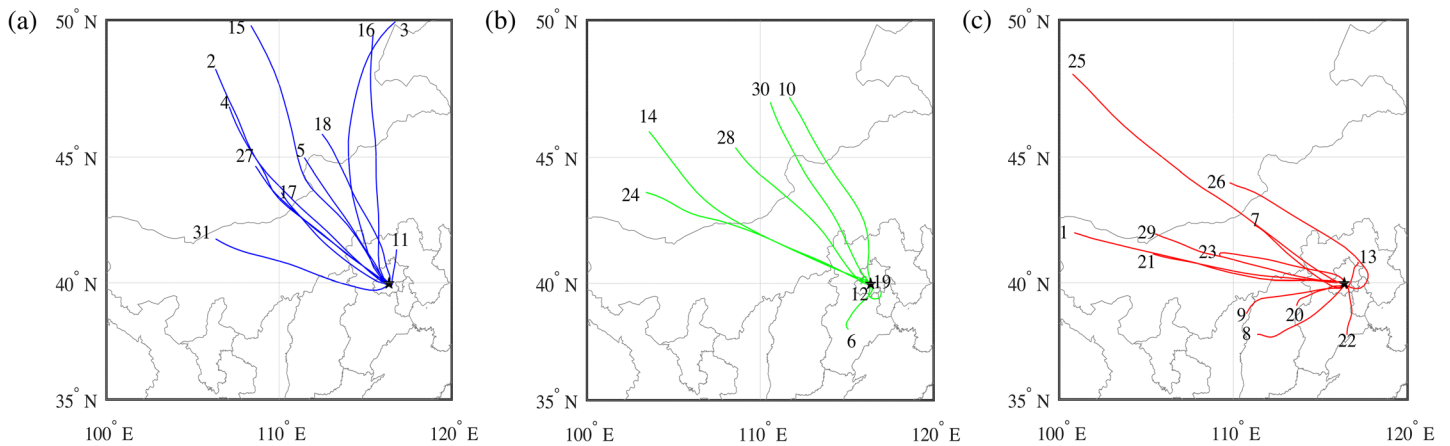


Figure 3. Twenty-four-hour back trajectories at 100 m height arriving at IAP site (star: 325 m tower) at 17:00 LST on different polluted days for the clean episodes (a), light PEs (b), and heavy PEs (c). The numbers indicate the day in December 2015.

The daily mean values of these four meteorological elements at different polluted levels were estimated. The daily mean WS/RH/pressure was $0.80 \text{ m s}^{-1}/31.06\%/1,024.04 \text{ hPa}$, $0.43 \text{ m s}^{-1}/45.52\%/1,023.74 \text{ hPa}$, and $0.30 \text{ m s}^{-1}/64.99\%/1,020.97 \text{ hPa}$ for clean, light, and heavy polluted conditions, respectively, showing that the WS decreased with increasing polluted levels. The largest air temperature (1.96°C) on the light polluted days was found, while clean (0.70°C) and heavy polluted days (0.79°C) had similar daily averaged air temperatures.

3.2. Characteristics of Meteorological Conditions at Different Levels

In this section, the averaged profiles of different meteorological factors averaged at noon time (12:00–14:00 LST, when solar radiation reaches the maximum value) and midnight (22:00–24:00 LST, which can capture more pollution samples in Figure 2) were used to investigate the different vertical variations of the UBL over Beijing under these three polluted conditions between daytime and nighttime. Note that the vertical variations of WS were not pronounced, and WS were below 2 m s^{-1} at all measured levels at the noontime of HPEs, while they significantly increased with height for LPEs and CEs (Figure 4). Compared to CEs, the WS (T) decreased (increased) throughout the observed heights, which ranged from 34.3% to 25.8% (36.6% to 375.7%) and increasing (decreasing) with evaluated height at LPEs (Figure 4). Significant temperature inversions were found during polluted nights, showing stable stratification in the nighttime UBL.

Figure 5 shows the diurnal change of the bulk Richardson number (Rb) calculated by the wind speed and air temperature averaged with two lower heights (32 and 47 m) and two higher heights (200 and 240 m), revealing that the stability of the atmosphere during polluted nights was more stable than those during clean nights. Moreover, this stable stratification occurred early at 15:00 LST and maintained and lasted for the whole nights during the HPEs. RH on heavy polluted days was far greater than the light and clean days at all observed levels due to an easterly wind with more moisture.

All the implications of variations in surface $\text{PM}_{2.5}$ and meteorological conditions can be summarized as follows: Southwesterly wind transports polluted air with high-concentration aerosols to Beijing, resulting in worse air quality during HPEs, while the strong northwesterly wind brought cold clean air to Beijing, resulting in removal of the local high-concentration aerosols and decrease in temperature with high RH during HPEs, which is consistent with the findings of previous studies (Li et al., 2017; Wang et al., 2013; Yang et al., 2018). This higher RH may further worsen aerosol pollution due to the hygroscopic growth effects of aerosols (Han et al., 2018; Sun et al., 2014). Additionally, the stable stratification UBL featured HPEs, which also plays an important role in the accumulation of polluted aerosols under HPEs (Miao et al., 2018; Zhong et al., 2017).

3.3. Characteristics of Flux Parameters at Different Levels

As an important quantity, u_* is used in numerical applications to parameterize the turbulent mixing process, and TKE is a direct measure of the turbulence intensity, which is essential for predicting air dispersion. The

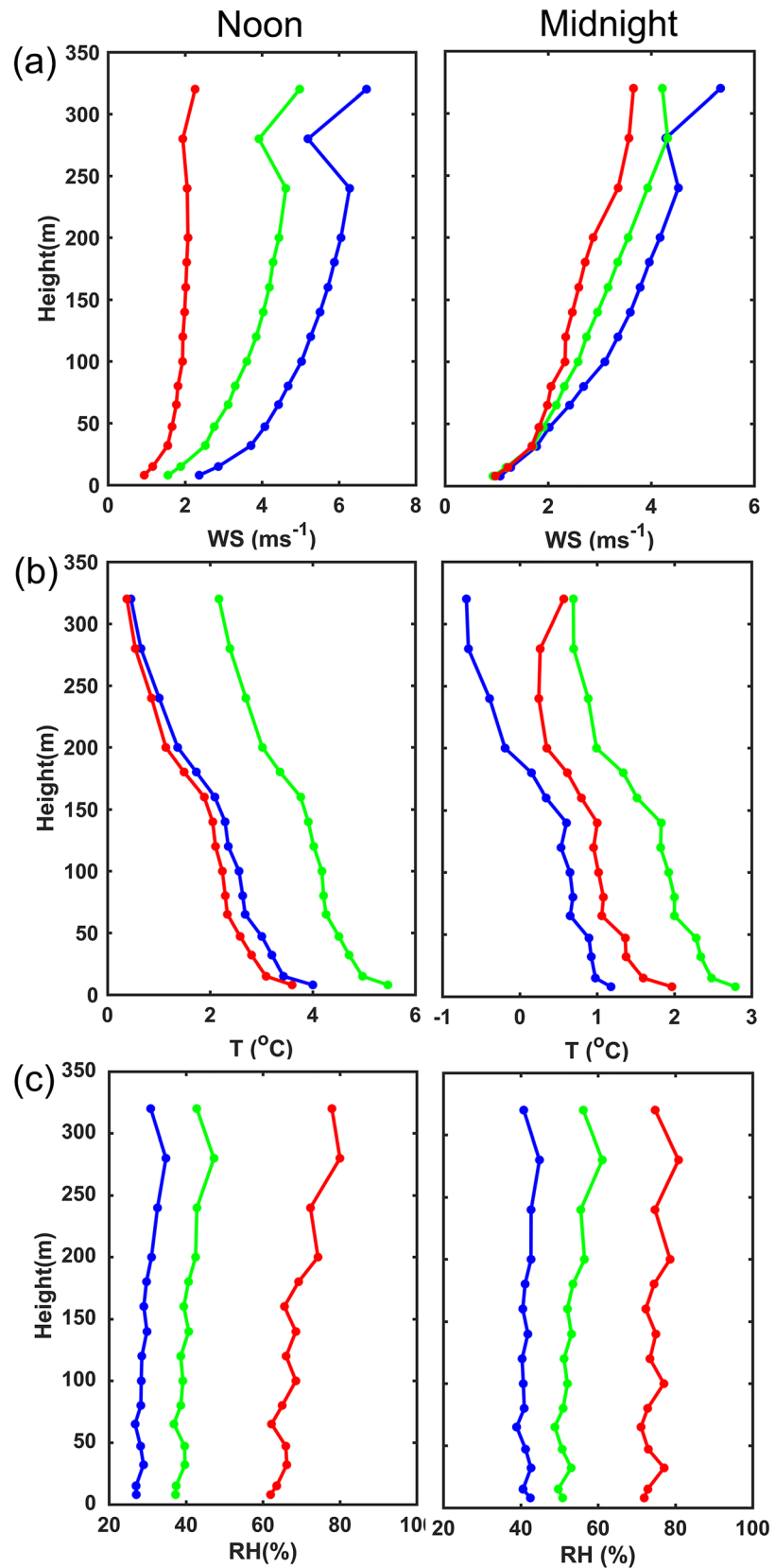


Figure 4. The average noon hours (12:00–14:00) and average midnight hours (22:00–24:00) vertical profiles, WS (a), air temperature (b), and RH (c) during clean episodes (blue), light PEs (green), and heavy PEs (red).

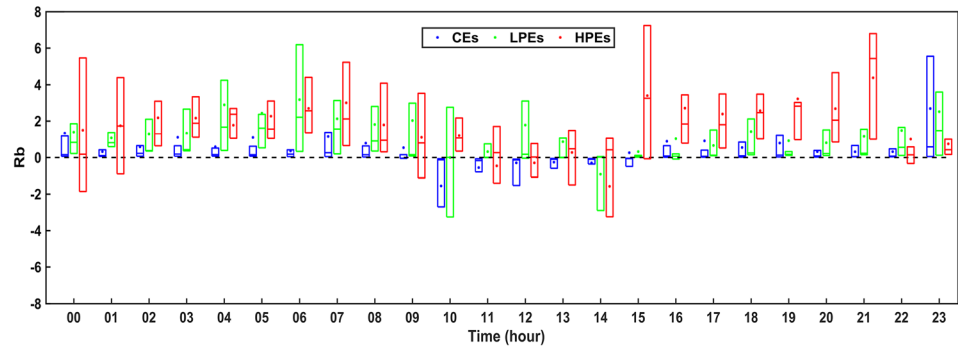


Figure 5. Box and whisker plots of bulk Richardson number at different levels in clean episodes (blue), light PEs (green), and heavy PEs (red). The top, middle, and bottom horizontal lines in the box represent the average, 75th percentile, and 25th percentile, respectively.

relationships between surface $PM_{2.5}$ concentrations and vertical flux dynamic factors (i.e., u_* and TKE in Figure S1) exhibited significant anticorrelations, which is consistent with the findings of previous studies (Dupont et al., 2016; Holmes et al., 2015; Liu, Gao, et al., 2019; Wang, Wang, et al., 2019). In detail, high concentrations of $PM_{2.5}$ at the ground were associated with weak u_* and TKE at all seven measured levels. The diurnal variations were not obvious, and values were lower than 0.25 m s^{-1} and $0.5 \text{ m}^2 \text{ s}^{-2}$ on heavy polluted days for both u_* and TKE at all levels (Figure 6). In contrast with daytime, a larger difference in u_* and TKE occurred during the nighttime between CEs and LPEs.

For vertical profiles averaged at noontime and midnight, increasing u_* was found at heights below 140 m, particularly below 80 m, and then slightly decreased upward of 140 m for all different polluted conditions (Figure 7). The same pattern occurred for TKE. For clean daytime, the slopes between u_* at 140 m and other

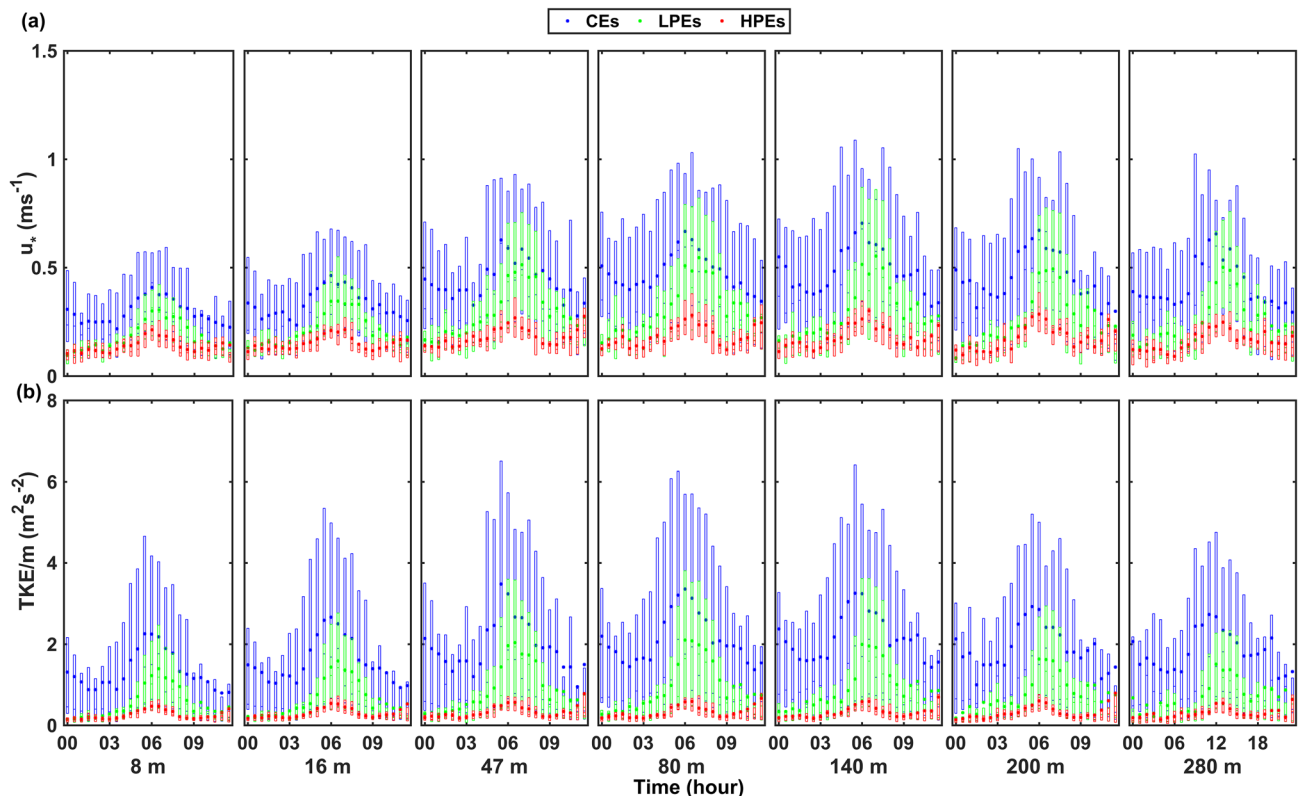


Figure 6. Similar to Figure 5 but for friction velocity (a) and turbulence kinetic energy (b) at different levels in clean episodes (blue), light PEs (green), and heavy PEs (red).

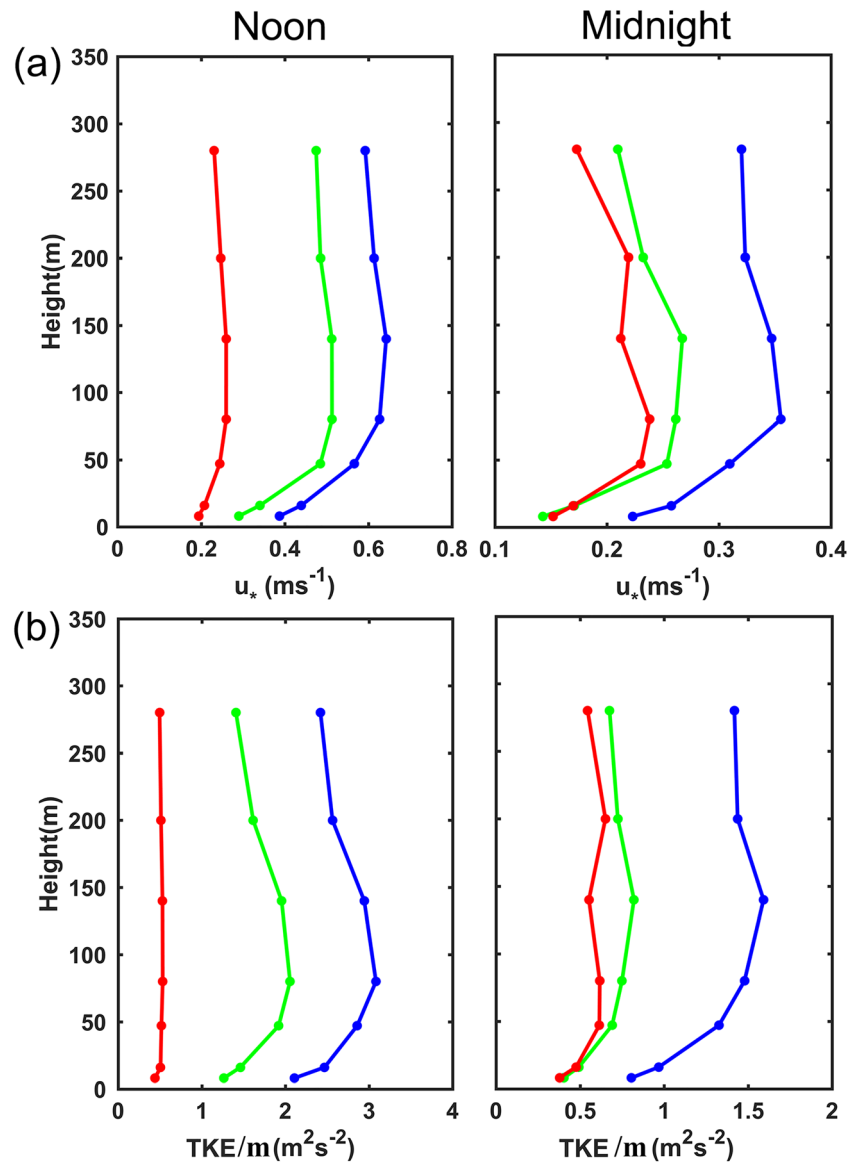


Figure 7. Similar to Figure 4 but for friction velocity (a) and turbulence kinetic energy (b).

levels of 8, 16, 47, 80, 200, and 280 m were estimated as 0.56, 0.64, 0.85, 0.92, 0.96, and 0.87, respectively, in this study. In contrast, u_* and TKE under heavy polluted conditions were very weak and showed unnoticeable vertical changes at noontime, in which values of u_* and TKE during daytime were weaker than under clean conditions during nighttime, as shown in Figure 6. In addition, maximum change magnitudes for u_* (0.38 m s^{-1}) occurred at the 140 m level between heavy polluted and clean conditions during daytime, while the largest attenuation ratio of 65.0% occurred at the 280 m level. For TKE, the variation ratios were similar at all levels. Differences in vertical changes in u_* and TKE between heavy and light pollution at midnight seemed nonobvious in contrast to the changes at noontime.

3.4. Characteristics of Radiation Balance at Different Levels

To explore the relationship between radiation and aerosol pollution, four components (i.e., DSR, USR, DLR, and ULR) of radiation at three height levels were collected. Taking the 140 m height as an example, Figure S2 presents an hourly scale time series of four components of radiation and net radiation during the studied period. Figure 8 shows the mean diurnal variation in these five radiation variables at 47, 140, and 280 m during CEs, LPEs, and HPEs, and the differences in these five variables between HPEs and

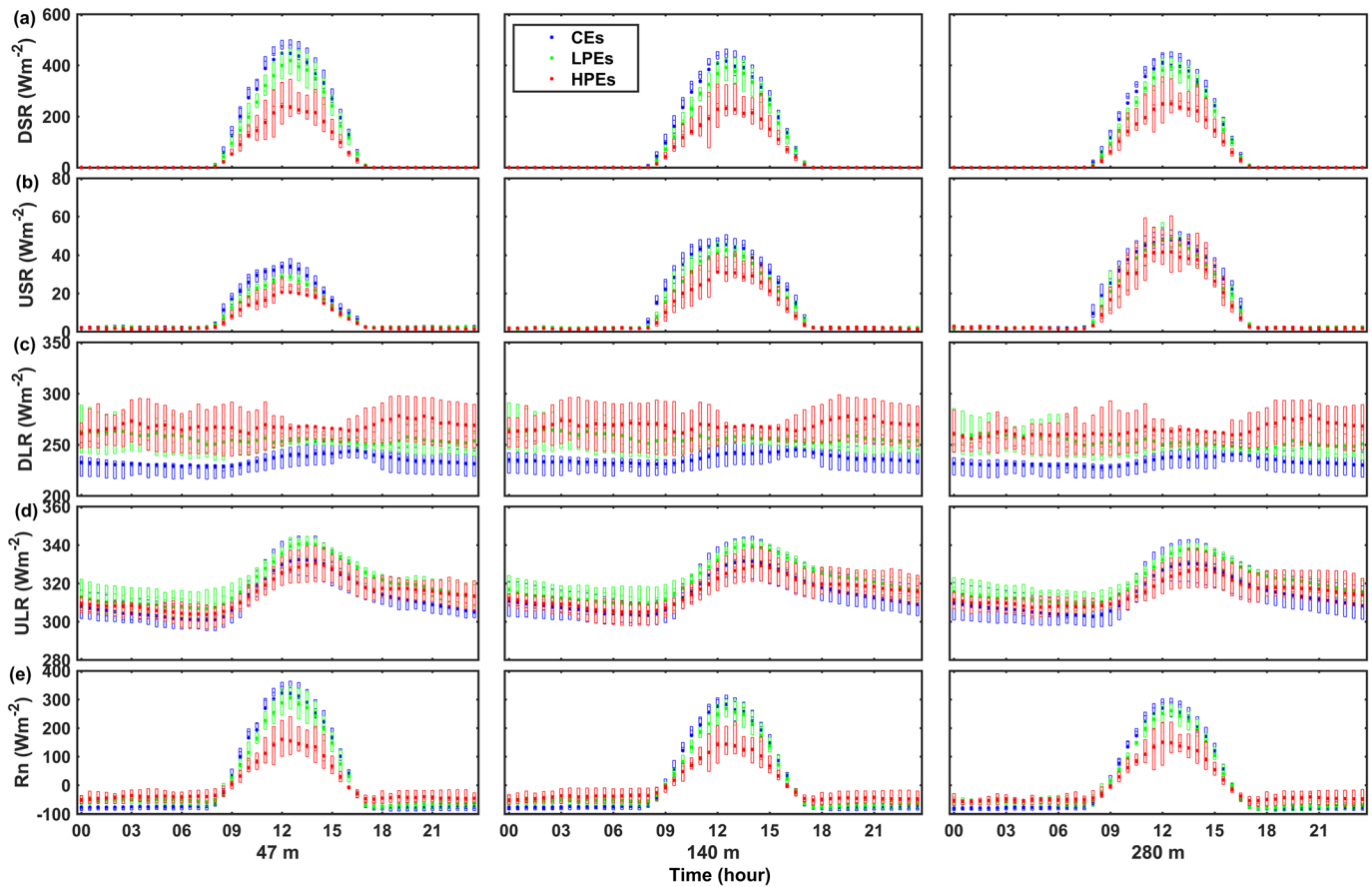


Figure 8. Similar to Figure 5 but for downward shortwave radiation (a), upward shortwave radiation (b), downward incoming longwave radiation (c), upward longwave radiation (d), and net radiation (e).

CEs are also shown in Figure 9. Generally, less shortwave radiation and more longwave radiation were received by the near-surface layer during the daytime of PEs than during the daytime of CEs. This reduced DSR implies the strong cooling effect of the aerosols at surface during HPEs mainly resulted in a lower air temperature, relative to the clean noon with a cold northerly wind in Beijing, with decrease ratios ranging from 9.8% to 17.4% at all measured heights (Figure 4b). The aerosol cooling radiative at surface is a negative feedback to the development of the UBL, which can further aggravate the accumulation of pollutants. This effect on the surface $PM_{2.5}$ concentration has also been quantified in sensitivity studies using the Weather Research and Forecasting with Chemistry (WRF-Chem) model in Wu et al. (2019). They found that when the near-surface $PM_{2.5}$ mass concentration increased from approximately $50 \mu\text{g m}^{-3}$ to hundreds $\mu\text{g m}^{-3}$, resultant cooling effects positively contributed to the accumulation of the $PM_{2.5}$ by more than 20% during the daytime.

The differences in four components between HPE and CEs were estimated as shown in Figure 9, which are defined as D_{DSR} , D_{USR} , D_{DLR} , and D_{ULR} , respectively. The largest D_{DSR} (D_{USR}) reached 210.4 (15.0) W m^{-2} at 11:00 (11:00) LST and 160.2 (11.1) W m^{-2} at 11:00 (10:30) LST (Figure 9a), and the attenuation ratios were approximately 54.3% (47.6%), 49.8% (43.3%), and 45.0% (26.5%) for the 47, 140, and 280 m levels, respectively. The maximum D_{DLR} between HPEs and CEs ranged from 42 to 46 W m^{-2} and occurred during nighttime (approximately 21:00 LST) at all three levels (Figure 9c). D_{ULR} was lower than 10 W m^{-2} between PEs and CEs. The difference in R_n (D_{R_n}) between PE and CE was also large and similar to D_{DSR} , with a maximum value (attenuation ratio) of 166.22 W m^{-2} (51.8%) at the 47 m level, 138.88 W m^{-2} (49.1%) at the 140 m level, and 119.33 W m^{-2} (44.3%) at the 280 m level, resulting in a larger albedo during HPEs (0.10, 0.15, and 0.18 at the 47, 140, and 280 m levels at noontime) than during CEs (0.08, 0.11, and 0.12 at the 47, 140, and 280 m levels at noontime).

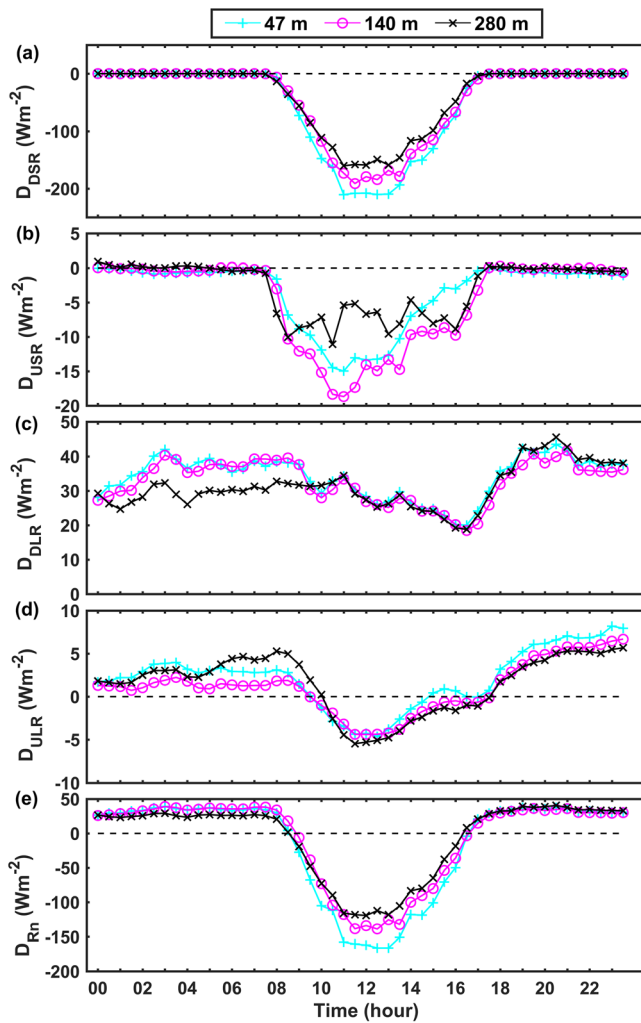


Figure 9. The mean diurnal variation in the difference in downward shortwave radiation (D_{DSR}) (a), upward shortwave radiation (D_{USR}) (b), downward longwave radiation (D_{DLR}) (c), upward longwave radiation (D_{ULR}) (d), and net radiation (D_{Rn}) (e) between heavy PEs and clean episodes at the 47 (green), 140 (purple), and 280 m (black) levels.

Center Business District of Beijing is located. The area averaged Q_f values were determined based on the flux source area of the 47, 140, and 280 m levels as 21.6 W m^{-2} , 20.4 W m^{-2} , and 16.3 W m^{-2} . Q_f can be the primary input of energy to the balance in winter over heterogeneous urban surfaces with high density buildings (Oke et al., 2017), especially during polluted winter with reduced R_n ($<150 \text{ W m}^{-2}$ at noon), as shown in Figure S2. The heat storage G was quantitatively derived by $R_n + Q_f - H - LE$, assuming the same Q_f during different days in this month.

Taking the 140 m level as an example, Figure S3 shows that the heat exchanges were obviously weak during PEs, and H was particularly dramatically attenuated in HPEs and the maximum values of H reached 300 W m^{-2} in CEs and below 100 W m^{-2} in HPEs. Note that during the red alert PEs from 19 to 24 December, H decreased along with the lasting polluted time, which indicates the feedback of the UBL to the polluted aerosol effect, especially in the last stage of the pollution process (22–24 December) with little changes in WS (Figure 2b) due to the reduction in the solar radiation at the near surface. This feedback is negative to the diffusion of the polluted aerosols. Such UBL-aerosol interactions have been discussed in previous field observations and experiments (Fan et al., 2019; Han et al., 2018; Quan et al., 2013; Wang, Liu, et al., 2019). Latent heat exchange was extremely weak, and LE was less than 50 W m^{-2} during the entire studied period in winter, mainly due to the large impervious urban surfaces of Beijing with a low water

Generally, the magnitude of D_{DSR} and D_{USR} decreased with evaluated height in the near-surface UBL, ranging from heights of 47 to 280 m (Figures 9a and 9b), implying that much more shortwave radiation is absorbed and scattered by the high-concentration aerosols in the UBL. Similarly, the magnitude of D_{DLR} (D_{ULR}) from late night to early morning decreased (increased) with evaluated height in the near-surface UBL (Figures 10c and 10d), suggesting that much more longwave radiation was trapped by the high-concentration aerosols in the UBL. The vertical variation in D_{Rn} mainly depended on the combination of D_{DSR} , D_{USR} , D_{ULR} , and D_{DLR} . Note that the different compositions of pollutants and sizes of particulate matter induced different longwave and shortwave radiation effects at the surface and top of the atmosphere (Gu et al., 2006; Ghan et al., 2012; Haywood & Boucher, 2000; Huang et al., 2018; Liu et al., 2018; Yang et al., 2020), which should be further explored at vertical near-surface UBL in Beijing in future studies, combined with vertical aerosol measurements.

Note that the covering of clouds also plays an important role in surface radiation. However, we are unable to exclude potential influences of clouds in this study because of the lack of accurate cloud observations. In particular, satellite observations may fail to distinguish aerosols and clouds on highly heavy polluted days (Tan et al., 2018). Moreover, previous studies reported that high aerosol loading could lead to enhancement of the cloud fraction (Gunthe et al., 2011; Li et al., 2016; Malavelle et al., 2017; Zhao et al., 2017), and during heavy polluted days, more clouds were indeed found over Beijing in case studies (Li et al., 2018; Wang, Liu, et al., 2019; Yang et al., 2020). Therefore, as one of features of HPEs, the existing clouds could be the result of polluted aerosols, which is outside of the scope of the present work.

3.5. Characteristics of the Heat Energy Budget at Different Levels

Figure 10 maps Q_f (month averaged) estimated by using the RAHF model during December 2015 around the 325 m tower ($20 \times 20 \text{ km}$) for Beijing. Consistent with the urban fraction shown in Figure 1c, a large impervious fraction accompanied large values of Q_f and vice versa. Generally, Q_f declined along the density gradients of urban development, from center to rural. The largest values of Q_f could reach approximately 130 W m^{-2} and are mostly distributed southeast of the 325 m tower, where the

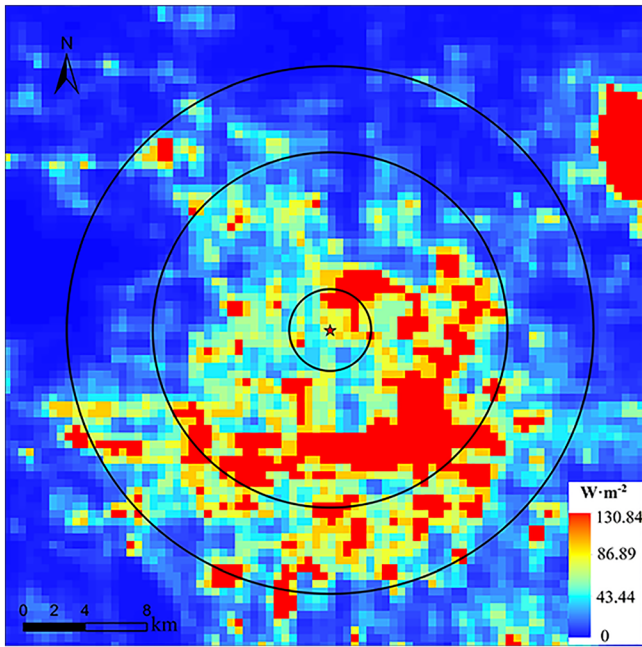


Figure 10. Spatial distributions of anthropogenic heat flux at a 500 m resolution during December 2015 around the 325 m tower (20×20 km) for Beijing (black circles from inner to outside indicate flux source areas for the 47, 140, and 280 m levels; red star: 325 m tower).

fraction, as shown in Table 2. Moreover, it is obvious that mostly urban fabrics released much more heat to the atmosphere during the nighttime for CEs than PEs. The largest amount of G during daytime (nighttime), approximately 270.8 (311.8) W m^{-2} , occurred at 12:00 (23:00) LST 17 (2) December, with a weak (strong) H and WS , approximately 31.6 (39.4) W m^{-2} and 1.2 (12.26) m s^{-1} at the 140 m level. In addition, G was also reduced for polluted conditions.

The diurnal variation in heat fluxes, H and LE , at all seven observed heights, and G at three heights for the three different polluted conditions are illustrated in Figure 11. Similar to the changes in the time series of 140 m, as mentioned above, compared to the PEs, CEs had stronger sensible heat exchange during the daytime at all levels. The mean values of LE were lower than 30 W m^{-2} in all three different polluted conditions at seven levels, which are much smaller in HPEs than LPES/CEs. Liu, Gao, et al. (2019) also reported that H on heavily polluted days (daily mean $\text{PM}_{2.5}$ concentration $> 150 \mu\text{g m}^{-3}$) was weaker than that on clean days (daily mean $\text{PM}_{2.5}$ concentration $< 75 \mu\text{g m}^{-3}$) in wintertime, at a rural site of mulched wheat in the North Plain of China, approximately 120 km away from the IAP station. The maximum soil heat storage during the daytime was approximately 100 W m^{-2} , and most of the soil released less than 50 W m^{-2} over the winter wheat surface in rural areas (Liu, Gao, et al., 2019). In contrast, the maximum (minimum) of G could reach over 200 W m^{-2} (-100 W m^{-2}) during the daytime (nighttime) for CEs and approximately 150 W m^{-2} (-50 W m^{-2}) for HPEs in the whole urban near-surface layer (Figure 11). Relative to rural areas, this larger heat sto-

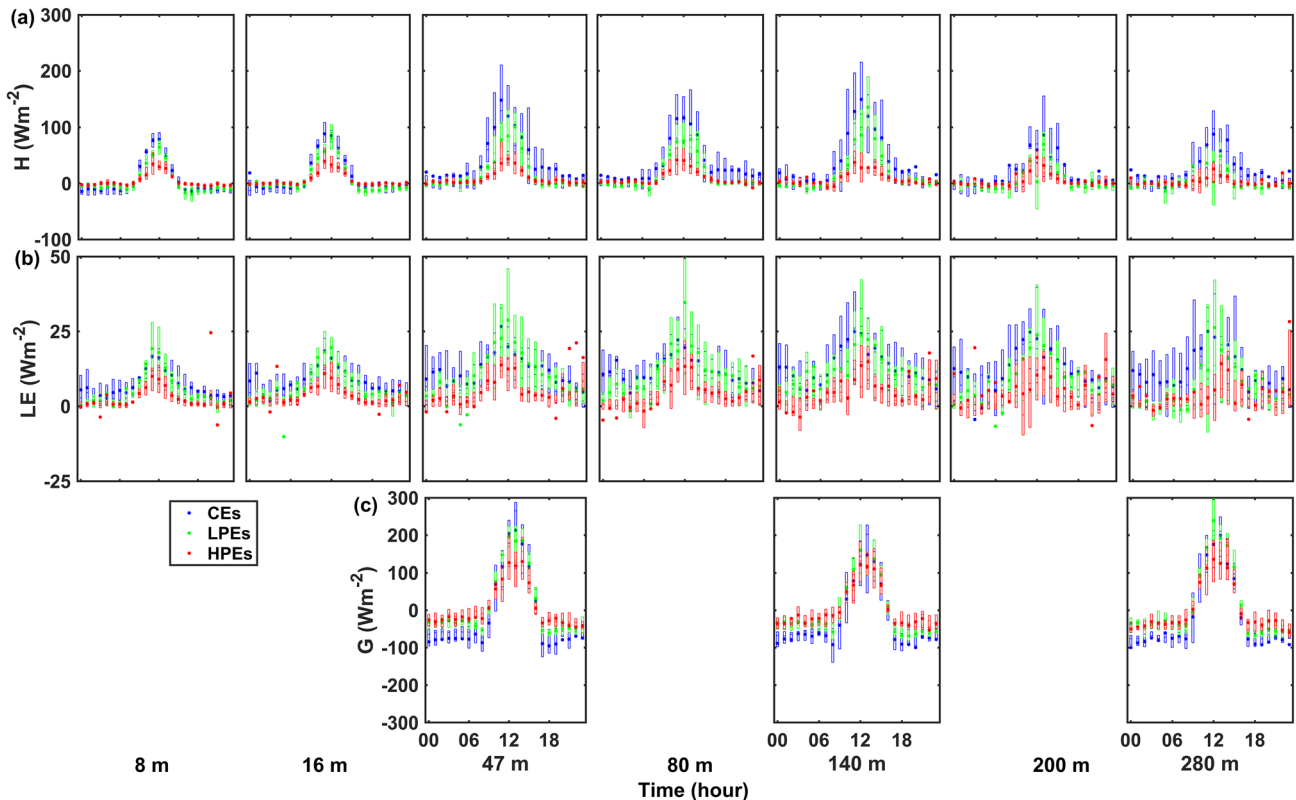


Figure 11. Similar to Figure 5 but for sensible heat flux (a), latent heat flux (b), and storage heat (c) at different levels.

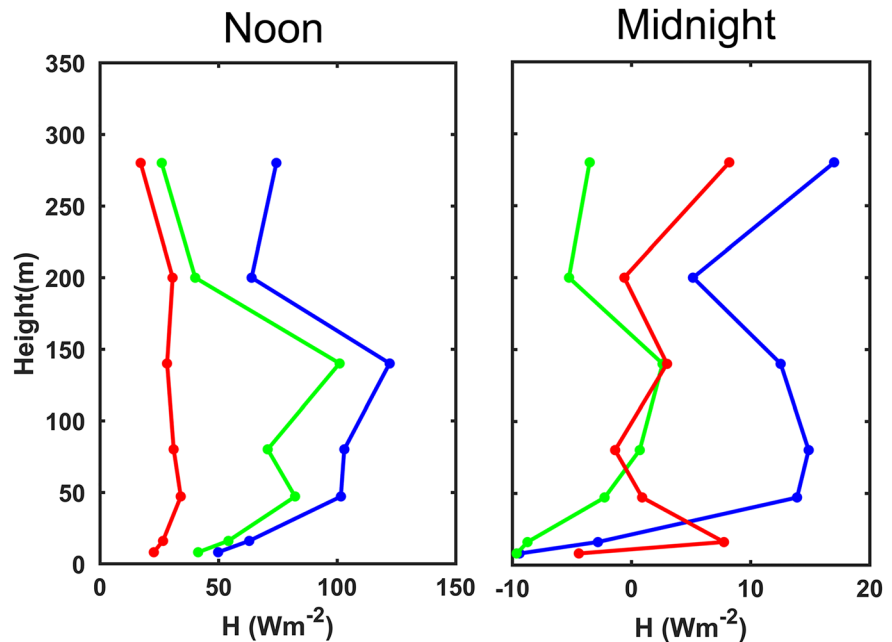


Figure 12. Similar to Figure 4 but for sensible heat flux.

range of urban surfaces is among the main causes of the urban heat island effect. Note that heat storage in both urban and rural areas dramatically modulated air pollution, and their interactions should be considered in numerical models, particularly in urban canopy models for accurate simulations of urban weather, climate, and environment.

For the vertical profile of H (Figure 12) during the clean daytime, the slopes between H at 140 m and other levels of 8, 16, 47, 80, 200, and 280 m were estimated as 0.32, 0.42, 0.77, 0.68, 0.39, and 0.23, respectively. A dramatic vertical change was found, especially between the 140 and 200 m levels for light polluted and clean noon, while a nonapparent vertical change was found for heavy polluted noon. Previous studies have shown that both the momentum and sensible heat fluxes increased with height from the surface up to the upper portion of the roughness sublayer (RSL) (Christen et al., 2009; Grimmond et al., 2004), while they naturally decreased by a small fraction (<10%) in the constant flux (Zou et al., 2017). According to the estimation of depth for RSL, typically 2–3 times the spatially averaged building height (Roth, 2000), we can speculate that the three levels, 8, 16, and 47 m, could be in the RSL, with an approximately 18.7 m height of the spatially averaged building around the 325 m tower (section 2.1). When combined with the slopes of u_* and H at different levels, it is hard to speculate whether or not the 80 or 200 m level is in the constant flux layer in this study, as the 280 m level is mostly in the mixing layer (Miao et al., 2012), and further research should be conducted with much longer term observation data.

Moreover, similar to u_* and TKE (Figure 7), H values in heavy polluted conditions were also much weaker and showed no noticeable vertical change at noontime. These results imply an insignificant dynamic effect under heavy polluted conditions during both daytime and nighttime, which is conducive to the accumulation of pollutants. In particular, polluted nighttime was usually accompanied by thermal inversion. Thus, the existence of both a weak dynamic effect and thermal inversion aggravates the transport condition of nocturnal pollutants, and the $PM_{2.5}$ concentration typically reaches a maximum at midnight, as shown in Figure 2a. In contrast, for H , the maximum magnitude was approximately 93.8 W m^{-2} at the 140 m level, and the attenuation ratio reached 76.8%, which is close to the largest ratio of 76.9% at the 280 m level. Differences in the vertical changes in u_* , TKE, and H between heavy and light pollution are midnight seemed nonobvious in contrast with changes at noontime. In general, these results may suggest a significant effect of high-concentration aerosols on the momentum and sensible heat fluxes in different layers of the UBL, with the maximum magnitudes in the constant flux layer and the largest variation ratio in the mixing layer.

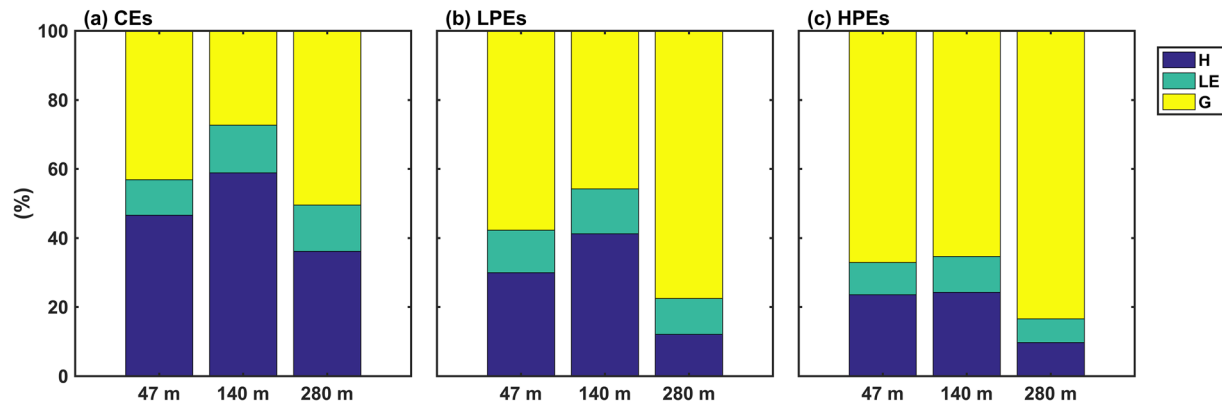


Figure 13. The partitions of the surface energy in clean episodes (a), light PEs (b), and heavy PEs (c) at the 47, 140, and 280 m levels.

To quantitatively investigate the characteristics of the surface energy partitions under different polluted conditions, the situations described by $H/(R_n + Q_p)$, $LE/(R_n + Q_p)$, and $G/(R_n + Q_p)$ averaged during daytime hours (08:00–17:00 LST) are shown in Figure 13. Generally, for UBL during wintertime, LE accounted for less than 16% of $R_n + Q_p$, which was mainly balanced by the other two terms. In detail, during clean episodes, H accounts for the absolute proportion, which is more than approximately 50%, of $R_n + Q_p$ for the 47 and 140 m levels, while H and G show similar proportions of 41.6% and 43.1%, respectively, for the 280 m levels. Values of G at all three levels had a positive relationship with pollution levels, accompanied by decreasing H , and approximately 82.4% of $R_n + Q_p$ was stored in the urban fabrics at the 280 m levels during heavy pollution episodes. Taking 140 m as an example, $H/(R_n + Q_p)$ was 58.9%, 41.3%, and 24.3%, while $G/(R_n + Q_p)$ was 27.3%, 45.8%, and 65.4% for CE, LPE, and HPE, respectively. A significant reduction in $H/(R_n + Q_p)$, an approximately 34.6% difference between clean and heavy pollution episodes, indicates extremely weak heat exchange, and much more heat is stored in urban fabrics under heavy pollution conditions. This event will suppress the evolution of the UBL and weaken the vertical mixing of the pollutants in the UBL. Based on the process analysis on assessing the formation and evolution mechanisms of severe haze pollution from 23 to 24 December 2015 (the same as one of the heavy pollution episodes in this study) in the Beijing-Tianjin-Hebei region using the WRF-Chem model, Chen, Zhu, et al. (2019) noted that restrained vertical mixing was the primary reason for the enhancement in surface $PM_{2.5}$ concentration, which is supported by our present observations.

Based on the SEB system, the changes in the available energy partition into sensible heat flux, latent heat flux, and heat storage can be mainly contributed by net radiation, air temperature, and WS, respectively. The former directly drives the SEB system, and the latter two imply ambient thermal conditions, advection, and convection efficiency (Sun et al., 2017). Figure 14 illustrates the changing of these three factors and SEB averaged for noon hours (12:00–14:00 LST) at the 140 m level during the entire study period, and the $PM_{2.5}$ concentrations were also averaged for noon hours in Figure 14c. Changes in $H/(R_n + Q_p)$ and $G/(R_n + Q_p)$ were nearly out of phase with each other because of the extremely weak LE and low $LE/(R_n + Q_p)$ during wintertime in Beijing. Generally, the variation in WS is positive (negative) to the proportion of H (G) in SEB. It was found that the coefficient of $H/(R_n + Q_p)$ and WS was approximately 0.4. On clean days, such as 2–5 December for example, $H/(R_n + Q_p)$ decreased with the weakening of WS. Under strong windy conditions ($WS \sim 11.2 \text{ m s}^{-1}$) at noon on 3 December, $H/(R_n + Q_p)$ was approximately 0.9 and $G/(R_n + Q_p)$ was negative, which means a super-high efficient heat exchange between the building and atmosphere, and $R_n + Q_p$ is insufficient for heat exchange; thus, heat storage becomes an energy supply for heating the atmosphere ($G < 0$), as shown in Figure S3c. For weak wind ($WS < 2 \text{ m s}^{-1}$) days in which all polluted events occurred, $G/(R_n + Q_p)$ was approximately 0.6 or greater. As another example, $G/(R_n + Q_p)$ on 22 December (a red alert issued) was close to 1.0, and this large partition (with a lower R_n compared to clean days) indicates a poor heat transfer as well as a remarkably poor UBL for vertical mixing of the pollutants. Note that the $PM_{2.5}$ concentration reached the largest value on 25 December, but H was not the weakest at that time. This is because vertical mixing is a major factor for the diffusion of pollutants, although not the only factor and other

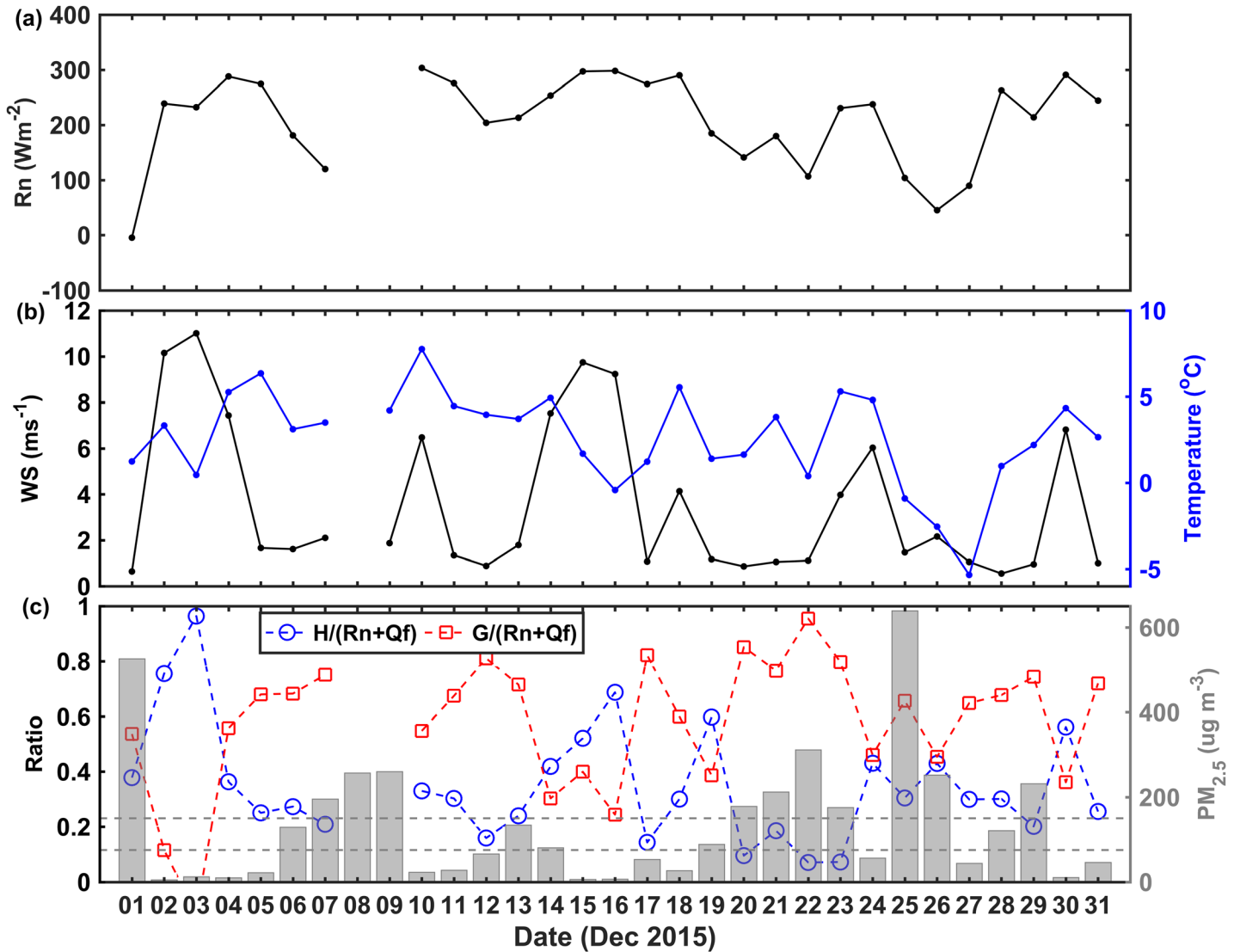


Figure 14. The noon hours (12:00–14:00 LST) averaged net radiation (a), wind speed and temperature (b), and partitions of sensible heat (blue) and storage heat (red) in the surface energy and noon hours surface $PM_{2.5}$ concentration (c) at the 140 m level.

physical and chemical processes (e.g., regional transport, secondary aerosol formation, and hygroscopic growth) also make a large contribution, as mentioned in section 3.1.

Previous studies revealed the characteristics of R_n and H under different polluted conditions (Liu, Gao, et al., 2019; Tang et al., 2016), while they did not further study the change in H/R_n under different polluted conditions. Following the results of Liu, Gao, et al. (2019), we further estimated H/R_n using the data collected over the winter wheat surface. Our work showed that H and R_n decreased by approximately 59.0% and 34.0% from clean days to heavy polluted days. In addition, the heat energy partitions were further calculated, and values of H/R_n were found to decrease from 44.8% to 30.1% and increased from 34.0% to 47.7% for $(R_n - H - LE)/R_n$, with WS reduced from 1.5 to 1.1 $m\ s^{-1}$ at the 4 m level.

Generally, combined with the different characteristics of SEB in different PEs, we can conclude that both R_n and H decreased, while the relative change in H was larger than that of R_n , resulting in a smaller H/R_n in PEs. This larger decrease in H was mainly attributed to the decreased WS under polluted conditions caused by the change in the synoptic condition. Holmes et al. (2015) also suggested that insufficient availability of net radiation energy and weak winds were responsible for the low magnitudes of latent and sensible heat fluxes. Therefore, it is better to investigate the UBL feedback to the existing polluted aerosols in the same

synoptic condition and quantitatively analyze the attributions of synoptic and polluted aerosols in the UBL under different synoptic conditions. In addition, UBL height is also an important factor linked to the variations in SEB and the pollution process, which should be considered in our future work when the high-resolution boundary layer height data are available.

4. Conclusions

Based on conventional meteorological, turbulence and radiation observations from the 325 m towers over the Beijing urban area, UBL characteristics, such as surface meteorological conditions, turbulent parameters, near-surface radiation balance, SEB, and vertical heat flux under different pollution conditions, were comparatively analyzed. The main conclusions can be summarized as follows.

First, compared to clean days, polluted days had weak wind, high humidity, and low air pressure. The warmest days occurred under light polluted conditions, and heavy polluted days exhibited significant aerosol cooling effects at surface and resultant lower air temperatures. The turbulence parameters and TKE/m (lower than 0.25 m s^{-1} and $0.5 \text{ m}^2 \text{ s}^{-2}$) at all measured levels were usually small under polluted conditions, indicating a nearly stagnant vertical mixing motion.

Moreover, relative to CEs, much more shortwave (longwave) radiation is absorbed and scattered (trapped) in the UBL during HPEs, leading to the fact that both downward and upward shortwave radiation (DSR and USR) dropped during daytime, while downward and upward longwave radiation (DLR and ULR) enhanced during nighttime on heavily polluted days. In the near-surface UBL, the drop magnitude of DSR and USR during daytime decreased with evaluated height, while the enhancement magnitude of DLR (ULR) at nighttime usually decreased (increased) with evaluated height. The vertical variation in net radiation mainly depended on the combination of changes in DSR, USR, ULR, and DLR.

Furthermore, heat storage G over the IAP site was quantitatively derived by the energy balance residual approach due to the available Q_f estimated by the RAHF model. Relative to CEs, both R_n and H decreased in the entire near-surface UBL during HPEs, with a larger relative change in H than R_n , leading to a smaller (larger) proportion of H (G in the urban fabrics) in $R_n + Q_f$. The remarkably weak wind may contribute to this larger relative change in H and the increase in G under polluted conditions. These results indicate not only the changes in polluted aerosols but also local weather conditions, accounting for the variations in energy partitions under different polluted conditions.

Finally, features of the vertical profiles of sensible heat flux and related meteorological elements and turbulence parameters can be concluded as follows: (i) WS, u_* , TKE, and H showed a nonapparent vertical change for heavy polluted noon, and (ii) a significant temperature inversion was found in HPEs midnight, and high RH ($> 60\%$) occurred at all the measured levels for heavy polluted days. (iii) The high-concentration polluted aerosols significantly affect the momentum and sensible heat fluxes in different layers of the UBL, with maximum effect magnitudes in the constant flux layer.

In general, our findings provide scientific evidence that the vertical characteristics of the radiation budget and heat budget process are closely related to surface aerosol pollution, which is expected to assist future modeling studies in improving the numerical model capability to accurately simulate the heat budget in the UBL under air pollution conditions. The findings reported here should also have important implications for other urban regions in both China and other developing countries experiencing high concentrations of $PM_{2.5}$ and with high building density.

Data Availability Statement

The data set used in this study is deposited at DOI: 10.17632/m7cngsdm8c.1.

References

- Barbaro, E., Vilà-Guerau de Arellano, J., Krol, M. C., & Holtslag, A. A. M. (2013). Impacts of aerosol shortwave radiation absorption on the dynamics of an idealized convective atmospheric boundary layer. *Boundary-Layer Meteorology*, *148*(1), 31–49. <https://doi.org/10.1007/s10546-013-9800-7>
- Brown, H., Liu, X. H., Feng, Y., Jiang, Y. Q., Wu, M. X., Lu, Z., et al. (2018). Radiative effect and climate impacts of brown carbon with the Community Atmosphere Model (CAM5). *Atmospheric Chemistry and Physics*, *18*(24), 17,745–17,768. <https://doi.org/10.5194/acp-18-17745-2018>

Acknowledgments

This work was funded by the National Key Research and Development Program of the Ministry of Science and Technology of China (2017YFC0209601 and 2016YFC0203304).

- Chan, C. K., & Yao, X. (2008). Air pollution in mega cities in China. *Atmospheric Environment*, *42*, 1–42. <https://doi.org/10.1016/j.atmosenv.2007.09.003>
- Che, H. Z., Shi, G. Y., Zhang, X. Y., Arimoto, R., Zhao, J. Q., Xu, L., et al. (2005). Analysis of 40 years of solar radiation data from China, 1961–2000. *Geophysical Research Letters*, *32*, L06803. <https://doi.org/10.1029/2004GL022322>
- Chen, B., Dong, L., Liu, X., Shi, G. Y., Chen, L., Nakajima, T., & Habib, A. (2016). Exploring the possible effect of anthropogenic heat release due to global energy consumption upon global climate: A climate model study. *International Journal of Climatology*, *36*, 4790–4796. <https://doi.org/10.1002/joc.4669>
- Chen, B., Dong, L., Shi, G. Y., Li, L., & Chen, L. (2014). Anthropogenic heat release: Estimation of global distribution and possible climate effect. *Journal of the Meteorological Society of Japan*, *92A*, 157–165. <https://doi.org/10.2151/jmsj.2015-060>
- Chen, B., & Shi, G. Y. (2012). Estimation of the distribution of global anthropogenic heat flux. *Atmospheric and Oceanic Science Letters*, *5*, 108–112. <https://doi.org/10.1080/16742834.2012.11446974>
- Chen, F., & Dudhia, J. (2001). Coupling an advanced land-surface/hydrology model with the Penn State/NCAR MM5 modeling system. Part I: Model implementation and sensitivity. *Monthly Weather Review*, *129*, 569–585. [https://doi.org/10.1175/1520-0493\(2001\)129<0569:CAALSH>2.0.CO;2](https://doi.org/10.1175/1520-0493(2001)129<0569:CAALSH>2.0.CO;2)
- Chen, L., Zhu, J., Liao, H., Gao, Y., Qiu, Y. L., Zhang, M. G., et al. (2019). Assessing the formation and evolution mechanisms of severe haze pollution in the Beijing–Tianjin–Hebei region using process analysis. *Atmospheric Chemistry and Physics*, *19*, 10,845–10,864. <https://doi.org/10.5194/acp-19-10845-2019>
- Chen, S. S., Hu, D., Wong, M. S., Ren, H., Cao, S., Yu, C., & Ho, H. C. (2019). Characterizing spatiotemporal dynamics of anthropogenic heat fluxes: A 20-year case study in Beijing–Tianjin–Hebei region in China. *Environmental Pollution*, *249*, 923–931. <https://doi.org/10.1016/j.envpol.2019.03.113>
- Chen, S. S., & Hu, D. Y. (2017). Parameterizing anthropogenic heat flux with an energy-consumption inventory and multi-source remote sensing data. *Remote Sensing*, *9*(11), 1165. <https://doi.org/10.3390/rs9111165>
- Cheng, X. L., Liu, X. M., Liu, Y. J., & Hu, F. (2018). Characteristics of CO₂ concentration and flux in the Beijing urban area. *Journal of Geophysical Research: Atmospheres*, *123*, 1785–1801. <https://doi.org/10.1002/2017JD027409>
- Christen, A., Rotach, M. W., & Vogt, R. (2009). The budget of turbulent kinetic energy in the urban roughness sublayer. *Boundary-Layer Meteorology*, *131*(2), 193–222. <https://doi.org/10.1007/s10546-009-9359-5>
- Detto, M., & Katul, G. G. (2007). Simplified expressions for adjusting higher-order turbulent statistics obtained from open path gas analyzers. *Boundary-Layer Meteorology*, *122*(1), 205–216. <https://doi.org/10.1007/s10546-006-9105-1>
- Dickerson, R. R., Kondragunta, S., Stenchikov, G., Civerolo, B. G., & Holben, B. N. (1997). The impact of aerosols on solar ultraviolet radiation and photochemical smog. *Science*, *278*(31). <https://doi.org/10.1126/science.278.5339.827>
- Dupont, J. C., Haefelin, M., Badosa, J., Elias, T., Favez, O., Petit, J. E., et al. (2016). Role of the boundary layer dynamics effects on an extreme air pollution event in Paris. *Atmospheric Environment*, *141*, 571–579. <https://doi.org/10.1016/j.atmosenv.2016.06.061>
- Fan, S. H., Gao, Z., Kalogiros, J., Li, Y. B., Yin, J., & Li, X. (2019). Estimate of boundary-layer depth in Nanjing City using aerosol lidar data during 2016–2017 winter. *Atmospheric Environment*, *205*, 67–77. <https://doi.org/10.1016/j.atmosenv.2019.02.022>
- Fu, Y. F., Zhu, J. C., Yang, Y. J., Yuan, R. M., Liu, G. S., Xian, T., & Liu, P. (2017). Grid-cell aerosol direct shortwave radiative forcing calculated by the SBDART model with MODIS and AERONET observations: An application study in winter and summer eastern China. *Advances in Atmospheric Sciences*, *34*(8), 952–964. <https://doi.org/10.1007/s00376-017-6226-z>
- Ghan, S. J., Liu, X., Easter, R. C., Zaveri, R., Rasch, P. J., Yoon, J.-H., & Eason, B. (2012). Toward a minimal representation of aerosols in climate models: Comparative decomposition of aerosol direct, semidirect, and indirect radiative forcing. *Journal of Climate*, *25*, 6461–6476. <https://doi.org/10.1175/JCLI-D-11-00650>
- Grimmond, C. S. B., Salmond, J. A., Oke, T. R., Offerle, B., & Lemonsu, A. (2004). Flux and turbulence measurements at a densely built-up site in Marseille: Heat, mass (water and carbon dioxide), and momentum. *Journal of Geophysical Research*, *109*, D24101. <https://doi.org/10.1029/2004JD004936>
- Gu, Y., Liou, K. N., Xue, Y., Mechoso, C. R., Li, W., & Luo, Y. (2006). Climatic effects of different aerosol types in China simulated by the UCLA general circulation model. *Journal of Geophysical Research*, *111*, D15201. <https://doi.org/10.1029/2005JD006312>
- Gu, Y., Wong, T. W., Law, C. K., Dong, G. H., Ho, K. F., Yang, Y. J., & Yim, S. H. L. (2018). Impacts of sectoral emissions in China and the implications: Air quality, public health, crop production, and economic costs. *Environmental Research Letters*, *13*, 084008. <https://doi.org/10.1088/1748-9326/aad138>
- Gunthe, S. S., Rose, D., Su, H., Garland, R. M., Achtert, P., Nowak, A., et al. (2011). Cloud condensation nuclei (CCN) from fresh and aged air pollution in the megacity region of Beijing. *Atmospheric Chemistry and Physics*, *11*, 11,023–11,039. <https://doi.org/10.5194/acp-11-11023-2011>
- Guo, J., He, J., Liu, H. L., Miao, Y. C., Liu, H., & Zhai, P. M. (2016). Impact of various emission control schemes on air quality using WRF-Chem during APEC China 2014. *Atmospheric Environment*, *140*, 311–319. <https://doi.org/10.1016/j.atmosenv.2016.05.046>
- Guo, J. P., Su, T. N., Chen, D. D., Wang, J., Li, Z. Q., Lv, Y. M., et al. (2019). Declining summertime local-scale precipitation frequency over China and the United States, 1981–2012: The disparate roles of aerosols. *Geophysical Research Letters*, *46*, 13,281–13,289. <https://doi.org/10.1029/2019GL085442>
- Guo, J. P., Zhang, X. Y., Wu, Y. R., Zhaxi, Y. Z., Che, H. Z., La, B., et al. (2011). Spatio-temporal variation trends of satellite-based aerosol optical depth in China during 1980–2008. *Atmospheric Environment*, *45*(37), 6802–6811. <https://doi.org/10.1016/j.atmosenv.2011.03.068>
- Han, S. Q., Hao, T. Y., Zhang, Y. F., Liu, J. L., Li, P. Y., Cai, Z. Y., et al. (2018). Vertical observation and analysis on rapid formation and evolutionary mechanisms of a prolonged haze episode over central-eastern China. *Science of the Total Environment*, *616–617*, 135–146. <https://doi.org/10.1016/j.scitotenv.2017.10.278>
- Haywood, J. M. (2011). Geostationary earth radiation budget intercomparison of longwave and shortwave radiation (GERBILS). *Quarterly Journal of the Royal Meteorological Society*, *137*, 1105–1105. <https://doi.org/10.1002/qj.884>
- Haywood, J. M. (2016). Atmospheric aerosols and their role in climate change, Climate change: Observed impacts on planet Earth. Second Edition, 449–463. <https://doi.org/10.1016/B978-0-444-63524-2.00027-0>
- Haywood, J. M., & Boucher, O. (2000). Estimates of the direct and indirect radiative forcing due to tropospheric aerosols: A review. *Reviews of Geophysics*, *38*(4), 513–543. <https://doi.org/10.1029/1999RG000078>
- Holmes, H. A., Sriramasamudram, J. K., Pardyjak, E. R., & Whiteman, C. D. (2015). Turbulent fluxes and pollutant mixing during wintertime air pollution episodes in complex terrain. *Environmental Science & Technology*, *49*, 13,206–13,214. <https://doi.org/10.1021/acs.est.5b02616>
- Holt, T. D., Niyogi, D., Chen, F., Manning, K., LeMone, M., & Qureshi, A. (2006). Effect of land-atmosphere interactions on IHOP 24–25 May 2002 convection case. *Monthly Weather Review*, *134*, 113–133. <https://doi.org/10.1175/MWR3057.1>

- Hsieh, C. I., Katual, G., & Chi, T. W. (2000). An approximate analytical model for footprint estimation of scalar fluxes in thermally stratified atmospheric flow. *Advances in Water Resources*, *23*(7), 765–772. [https://doi.org/10.1016/S0309-1708\(99\)00042-1](https://doi.org/10.1016/S0309-1708(99)00042-1)
- Hu, N., & Liu, X. M. (2013). A modeling study of the effect of anthropogenic aerosols on drought in the late spring of south China. *Acta Meteorologica Sinica*, *27*(5), 701–715. <https://doi.org/10.1007/s13351-013-0506-z>
- Huang, X., Wang, Z. L., & Ding, A. J. (2018). Impact of aerosol-PBL interaction on haze pollution: Multiyear observational evidences in North China. *Geophysical Research Letters*, *45*, 8596–8603. <https://doi.org/10.1029/2018GL079239>
- Jacobson, M., Kaufman, Y. J., & Rudich, Y. (2007). Examining feedbacks of aerosols to urban climate with a model that treats 3-D clouds with aerosol inclusions. *Journal of Geophysical Research*, *112*, D24205. <https://doi.org/10.1029/2007JD008922>
- Johnson, B. T., Haywood, J. M., & Hawcroft, M. K. (2019). Are changes in atmospheric circulation important for black carbon aerosol impacts on clouds, precipitation, and radiation? *Journal of Geophysical Research: Atmospheres*, *124*, 7930–7950. <https://doi.org/10.1029/2019JD030568>
- Kotthaus, S., & Grimmond, C. S. B. (2014). Energy exchange in a dense urban environment—Part I: Temporal variability of long-term observations in central London. *Urban Climate*, *10*, 261–280. <https://doi.org/10.1016/j.uclim.2013.10.002>
- Li, D., & Bou-Zeid, E. (2014). Quality and sensitivity of high-resolution numerical simulation of urban heat islands. *Environmental Research Letters*, *9*(5), 055001. <https://doi.org/10.1088/1748-9326/9/5/055001>
- Li, J., Sun, J. L., Zhou, M. Y., Cheng, Z. G., Li, Q. C., Cao, X. Y., & Zhang, J. J. (2018). Observational analyses of dramatic developments of a severe air pollution event in the Beijing area. *Atmospheric Chemistry and Physics*, *18*, 3919–3935. <https://doi.org/10.5194/acp-18-3919-2018>
- Li, Z., Lau, W. K.-M., Ramanathan, V., Wu, G., Ding, Y., Manoj, M. G., et al. (2016). Aerosol and monsoon climate interactions over Asia. *Reviews of Geophysics*, *54*, 866–929. <https://doi.org/10.1002/2015RG000500>
- Li, Z. Q., Guo, J. P., Ding, A. J., Liao, H., Liu, J. J., Sun, Y. L., et al. (2017). Aerosol and boundary-layer interactions and impact on air quality. *National Science Review*, *4*, 810–833. <https://doi.org/10.1093/nsr/nwx117>
- Ling, X. L., Guo, W. D., Fu, C., & B. (2014). Composite analysis of impacts of dust aerosols on surface atmospheric variables and energy budgets in a semiarid region of China. *Journal of Geophysical Research: Atmospheres*, *119*, 3107–3123. <https://doi.org/10.1002/2013JD020274>
- Liu, C., Chung, C. E., Yin, Y., & Schnaiter, M. (2018). The absorption Ångström exponent of black carbon: From numerical aspects. *Atmospheric Chemistry and Physics*, *18*, 6259–6273. <https://doi.org/10.5194/acp-18-6259-2018>
- Liu, C. W., Gao, Z. Q., Li, Y. B., Gao, C. Y., Su, Z. B., & Zhang, X. Y. (2019). Surface energy budget observed for a winter wheat field site in the north China plain during a fog-haze event. *Boundary-Layer Meteorology*, *170*, 489–505. <https://doi.org/10.1007/s10546-018-0407-x>
- Liu, J. K., Gao, Z. Q., Wang, L. L., Li, Y. B., & Gao, C. Y. (2017). The impact of urbanization on wind speed and surface aerodynamic characteristics in Beijing during 1991–2011. *Meteorology and Atmospheric Physics*, *130*(3), 311–324. <https://doi.org/10.1007/s00703-017-0519-8>
- Lolli, S., Khor, W. Y., Matjafri, M. Z., & Lim, H. S. (2019). Monsoon season quantitative assessment of biomass burning clear-sky aerosol radiative effect at surface by ground-based Lidar observations in Pulau Pinang, Malaysia in 2014. *Remote Sensing*, *11*(22), 1–14. <https://doi.org/10.3390/rs11222660>
- Luan, T., Guo, X. L., Guo, L. J., & Zhang, T. H. (2018). Quantifying the relationship between PM_{2.5} concentration, visibility and planetary boundary layer height for long-lasting haze and fog-haze mixed events in Beijing. *Atmospheric Chemistry and Physics*, *18*, 203–225. <https://doi.org/10.5194/acp-18-203-2018>
- Malavelle, F. F., Haywood, J. M., Jones, A., Gettelman, A., Clarisse, L., Bauduin, S., et al. (2017). Strong constraints on aerosol-cloud interactions from volcanic eruptions. *Nature*, *546*(7659), 485–491. <https://doi.org/10.1038/nature22974>
- Miao, S. G., Chen, F., Lemone, M. A., Tewari, M., Li, Q. C., & Wang, Y. C. (2009). An observational and modeling study of characteristics of urban heat island and boundary layer structures in Beijing. *Journal of Applied Meteorology and Climatology*, *48*(3), 484–501. <https://doi.org/10.1175/2008JAMC1909.1>
- Miao, S. G., Dou, J. X., Chen, F., Li, J., & Li, A. G. (2012). Analysis of observations on the urban surface energy balance in Beijing. *Science China Earth Sciences*, *55*(11), 1881–1890. <https://doi.org/10.1007/s11430-012-4411-6>
- Miao, Y. C., Guo, J. P., Liu, S. H., Zhao, C., Li, X. L., Zhang, G., et al. (2018). Impacts of synoptic condition and planetary boundary layer structure on the trans-boundary aerosol transport from Beijing-Tianjin-Hebei region to northeast China. *Atmospheric Environment*, *181*, 1–11. <https://doi.org/10.1016/j.atmosenv.2018.03.005>
- Miao, Y. C., Hu, X. M., Liu, S. H., Qian, T. T., Xue, M., Zheng, Y. J., & Wang, S. (2015). Seasonal variation of local atmospheric circulations and boundary layer structure in the Beijing-Tianjin-Hebei region and implications for air quality. *Journal of Advances in Modeling Earth Systems*, *7*, 1602–1626. <https://doi.org/10.1002/2015MS000522>
- Oke, T. R., Mills, G., Christen, A., & Voegt, J. A. (2017). *Urban climates*. Cambridge: Cambridge University Press.
- Quan, J. N., Gao, Y., Zhang, Q., Tie, X. X., Cao, J. J., Han, S. Q., et al. (2013). Evolution of planetary boundary layer under different weather conditions, and its impact on aerosol concentrations. *Particuology*, *11*(1), 34–40. <https://doi.org/10.1016/j.partic.2012.04.005>
- Roth, M. (2000). Review of atmospheric turbulence over cities. *Quarterly Journal of the Royal Meteorological Society*, *126*, 941–990. <https://doi.org/10.1256/smsqj.56408>
- Sellers, P., Los, S. O., Tucker, C. J., Justice, C. O., Dazlich, D. A., Collatz, G. J., & Randall, D. A. (1996). A revised land surface parameterization (SiB2) for atmospheric GCMs. Part II: The generation of global fields of terrestrial biophysical parameters from satellite data. *Journal of Climate*, *9*, 706–737. [https://doi.org/10.1175/1520-0442\(1996\)009<0706:ARLSPF>2.0.CO;2](https://doi.org/10.1175/1520-0442(1996)009<0706:ARLSPF>2.0.CO;2)
- Shi, Y., Hu, F., Fan, G. Q., & Zhang, Z. (2019). Multiple technical observations of the atmospheric boundary layer structure of a red-alert haze episode in Beijing. *Atmospheric Measurement Techniques*, *12*, 4887–4901. <https://doi.org/10.5194/amt-12-4887-2019>
- Su, T. N., Li, Z. Q., & Kahn, R. (2018). Relationships between the planetary boundary layer height and surface pollutants derived from lidar observations over China: Regional pattern and influencing factors. *Atmospheric Chemistry and Physics*, *18*, 15,921–15,935. <https://doi.org/10.5194/acp-18-15921-2018>
- Sun, T., Kotthaus, S., Li, D., Ward, H. C., Gao, Z., Ni, G.-H., & Grimmond, C. S. B. (2017). Attribution and mitigation of heat wave-induced urban heat storage change. *Environmental Research Letters*, *12*, 11,4007. <https://doi.org/10.1088/1748-9326/aa922a>
- Sun, Y. L., Jiang, Q., Wang, Z. F., Fu, P. Q., Li, J., Yang, T., & Yin, Y. (2014). Investigation of the sources and evolution processes of severe haze pollution in Beijing in January 2013. *Journal of Geophysical Research: Atmospheres*, *119*, 4380–4398. <https://doi.org/10.1002/2014JD021641>
- Taha, H. (1997). Urban climates and heat islands: Albedo, evapotranspiration, and anthropogenic heat. *Energy and Buildings*, *25*(2), 99–103. [https://doi.org/10.1016/S0378-7788\(96\)00999-1](https://doi.org/10.1016/S0378-7788(96)00999-1)

- Tan, S. C., Zhang, X., Wang, H., Chen, B., Shi, G. Y., & Shi, C. (2018). Comparisons of cloud detection among four satellite sensors on severe haze days in eastern China. *Atmospheric and Oceanic Science Letter*, *11*, 86–93.
- Tang, G. Q., Zhang, J. Q., Zhu, X. W., Song, T., Munkel, C., Hu, B., et al. (2016). Mixing layer height and its implications for air pollution over Beijing, China. *Atmospheric Chemistry and Physics*, *16*, 2459–2475. <https://doi.org/10.5194/acp-16-2459-2016>
- Wang, L., & Li, D. (2019). Modulation of the urban boundary layer heat budget by a heat wave. *Quarterly Journal of the Royal Meteorological Society*, *145*, 1814–1831. <https://doi.org/10.1002/qj.3526>
- Wang, L. L., Li, D., Gao, Z. Q., Sun, T., Guo, X. F., & Bou-Zeid, E. (2014). Turbulent transport of momentum and scalars above an urban canopy. *Boundary-Layer Meteorology*, *150*, 485–511. <https://doi.org/10.1007/s10546-013-9877-z>
- Wang, L. L., Liu, J. K., Gao, Z. Q., Li, Y. B., Huang, M., Fan, S. H., et al. (2019). Vertical observations of the atmospheric boundary layer structure over Beijing urban area during air pollution episodes. *Atmospheric Chemistry and Physics*, *19*(10), 6949–6967. <https://doi.org/10.5194/acp-19-6949-2019>
- Wang, L. L., Wang, H., Liu, J. K., Gao, Z. Q., Yang, Y. J., Zhang, X., et al. (2019). Impacts of the near-surface urban boundary layer structure on PM_{2.5} concentrations in Beijing during winter. *Science of the Total Environment*, *669*, 493–504. <https://doi.org/10.5194/acp-2018-1184>
- Wang, T. J., Jiang, F., Deng, J. J., Shen, Y., Fu, Q. Y., Wang, Q., et al. (2012). Urban air quality and regional haze weather forecast in Yangtze River Delta of China. *Atmospheric Environment*, *58*, 70–83. <https://doi.org/10.1016/j.atmosenv.2012.01.014>
- Wang, X. H., Miao, S. G., & Dou, J. X. (2018). Numerical simulation of the influence of aerosol radiation effect on urban boundary layer. *Science China Earth Sciences*, *61*(12), 1844–1858. <https://doi.org/10.1007/s11430-018-9260-0>
- Wang, X. R., Miao, S. G., Dou, J. X., Dong, P., & Wang, J. L. (2016). Observation and analysis of the air pollution impacts on radiation balance of urban and suburb areas in Beijing. *Chinese Journal of Geophysics (in Chinese)*, *59*(11), 3996–4006. <https://doi.org/10.6038/cjg20161106>
- Wang, Z. F., Li, J., Wang, Z., Yang, W. Y., Tang, X., Ge, B. Z., et al. (2013). Modeling study of regional severe hazes over mid-eastern China in January 2013 and its implications on pollution prevention and control. *Science China Earth Sciences*, *57*, 3–13. <https://doi.org/10.1007/s11430-013-4793-0>
- Wilczak, J. M., Oncley, S. P., & Stage, S. A. (2001). Sonic anemometer tilt correction algorithms. *Boundary-Layer Meteorology*, *99*(1), 127–150. <https://doi.org/10.1023/A:1018966204465>
- Wu, J. R., Bei, N. F., Hu, B., Liu, S. X., Zhou, M., Wang, Q. Y., et al. (2019). Aerosol–radiation feedback deteriorates the wintertime haze in the North China Plain. *Atmospheric Chemistry and Physics*, *19*, 8703–8719. <https://doi.org/10.5194/acp-19-8703-2019>
- Yang, Y., Zheng, Z. F., Yim, S. H. L., Roth, M., Ren, G. Y., Gao, Z. Q., et al. (2020). PM_{2.5} pollution modulates wintertime urban-heat-island intensity in the Beijing-Tianjin-Hebei megalopolis, China. *Geophysical Research Letters*, *47*(1), <https://doi.org/10.1029/2019GL084288>
- Yang, Y. J., Zheng, X. Y., Gao, Z. Q., Wang, H., Wang, T. J., Li, Y. B., et al. (2018). Long-term trends of persistent synoptic circulation events in planetary boundary layer and their relationships with haze pollution in winter half year over eastern China. *Journal of Geophysical Research: Atmospheres*, *123*, 10,991–11,007. <https://doi.org/10.1029/2018JD028982>
- Yim, S. H. L., Wang, M. Y., Gu, Y., Yang, Y., Dong, G. H., & Li, Q. (2019). Effect of urbanization on ozone and resultant health effects in the Pearl River Delta Region of China. *Journal of Geophysical Research: Atmospheres*, *124*, 11,568–11,579. <https://doi.org/10.1029/2019JD030562>
- Zhang, X. Y., Sun, J. Y., Wang, Y. Q., Li, W. J., Zhang, Q., Wang, W. G., et al. (2013). Factors contributing to haze and fog in China. *Chinese Science Bulletin*, *58*(13), 1178. <https://doi.org/10.1360/972013-150>
- Zhang, X. Y., Wang, Y. Q., Niu, T., Zhang, X. C., Gong, S. L., Zhang, Y. M., & Sun, J. Y. (2012). Atmospheric aerosol compositions in China: Spatial/temporal variability, chemical signature, regional haze distribution and comparisons with global aerosols. *Atmospheric Chemistry and Physics*, *12*, 779–799. <https://doi.org/10.5194/acp-12-779-2012>
- Zhao, B., Liou, K. N., Gu, Y., Li, Q., Jiang, J. H., Su, H., et al. (2017). Enhanced PM_{2.5} pollution in China due to aerosol-cloud interactions. *Scientific Reports*, *7*(1), 4453. <https://doi.org/10.1038/s41598-017-04096-8>
- Zheng, Z. F., Ren, G. Y., Wang, H., Dou, J. X., Gao, Z. Q., Duan, C. F., et al. (2018). Relationship between fine particle pollution and the urban Heat Island in Beijing, China: Observational evidence. *Boundary-Layer Meteorology*, *169*(1), 93–113. <https://doi.org/10.1007/s10546-018-0362-6>
- Zhong, J. T., Zhang, X. Y., Wang, Y. Q., Sun, J. Y., Zhang, Y. M., Wang, J. Z., et al. (2017). Relative contributions of boundary-layer meteorological factors to the explosive growth of PM_{2.5} during the red-alert heavy pollution episodes in Beijing in December 2016. *Journal of Meteorological Research*, *31*(5), 809–819. <https://doi.org/10.1007/s13351-017-7088-0>
- Zou, J., Zhou, B. W., & Sun, J. N. (2017). Impact of eddy characteristics on turbulent heat and momentum fluxes in the urban roughness sublayer. *Boundary-Layer Meteorology*, *164*(1), 39–62. <https://doi.org/10.1007/s10546-017-0244-3>